PAUL SCHERRER INSTITUT

PSI

O₂

CO₂

R·

HO₂

hv
Fe (III)carb
carboxyl
Fe (III)

H₂O₂

I⁻
HOI
I₂

IO₃⁻

Fenton

Fe (II)

O₃, I₂,
IO, HOI

Annual Report 2021

Laboratory of Environmental Chemistry

On the cover page:

Iodine chemistry affects the ozone budget in the atmosphere.

Central figure: Cycling of iodine species between the particle phase and the gas phase determines the fraction remaining and deposited in the troposphere and that reaching the stratosphere. Cycling is driven by redox processes, e.g., by iron (III) carboxylate photolysis driven radical chemistry, or by oxidants (e.g., ozone (O_3)) taken up from the gas phase.

In 2021, a campaign was conducted in collaboration with the University of Colorado in Boulder (UCB) (photo of a social event, bottom left). UCB brought along a cavity enhanced differential optical absorption spectroscopy (CE-DOAS) setup operating in the green and blue for the detection of iodine (I_2) and iodine oxide (IO) radicals (upper left). Experiments were performed with aerosol proxy materials as a thin film in coated wall flow tube experiments, which required handling light sensitive iron (III) complexes (upper right). Molecular dynamics simulations support kinetic experiments of the reaction of O_3 with iodide ions in aqueous solution. A snapshot (bottom right) shows the O_2 and IO^- products at the verge of the dissociation of the iodide ozonide intermediate. Liquid jet X-ray photoelectron spectroscopy to understand the surface propensity of different iodine species involved reference solutions of triiodide (I_3^-) (bottom far right).

Annual Report 2021

Laboratory of Environmental Chemistry

Editors

M. Schwikowski, M. Ammann

TABLE OF CONTENT

Analytical Chemistry

EDITORIAL

The year 2021 was again a challenging one for our Laboratory of Environmental Chemistry (LUC). COVID-related limited access to PSI continued to varying degrees throughout the whole year. Although remote tools were in place and managing lab times and home-office became routine, we still missed a lot the effortless exchanges in the coffee-round or the corridor.

Nevertheless we are proud of the research outcome we produced with overall 29 papers in peer-reviewed scientific journals. One highlight is an in-situ X-ray spectromicroscopic study showing that photolytically produced radicals can persist in viscous aerosol particles due to limited diffusive transport of O_2 (P. Alpert et al., page 9 of this report). Another exciting achievement is that a compilation of ice–core based aerosol records covering the last 250 years was published in the new report of the Intergovernmental Panel on Climate Change (IPCC AR6). Such records are indispensable to constrain model simulations of global aerosol radiative forcing, and we are pleased that the majority of the records was produced by our Analytical Chemistry Group (page 30).

The Surface Chemistry Group was very active at using the SLS facility at PSI for XPS and X-ray spectromicroscopic studies during 12 beamtimes; four of them at the Pollux and eight at the ISS beamline. At the latter also 10 beamtimes for external users were supported. After a major administrative effort caused by the constantly changing pandemic restrictions, the surface chemistry group was extremely pleased that they could host scientists from CU Boulder for an iodine campaign (see front page).

The Analytical Chemistry Group managed to conduct two successful ice core drilling campaigns in 2021. The first on Adamello glacier, which is the largest glacier in Italy. Bedrock was reached at 224 m depth, which is to my best knowledge a new record for ice core drilling in the Alps (p. 24). The second campaign was on Colle Gnifetti, Monte Rosa, where two parallel cores down to bedrock at 82 m and two shallow cores were collected (p. 22 and 23). This is probably the last ice core site in the Alps, which is because of its high elevation not affected by melting yet. The bedrock cores were recovered in the frame of the ICE MEMORY project.

On 10 November 2021 Huanyu Yang successfully defended his PhD entitled "Hydrogen Bonding structure of Water at Interfaces relevant for ice nucleation" at the ETH Zürich. Congratulations!

Already early in the year we as main organizers decided to postpone for a second time the 3rd Open Science Conference of the International Partnerships in Ice Core Sciences (IPICS), which should have been held in October 2021 in Crans-Montana. It will now take place this year from 2 to 7 October, and we are looking forward to welcoming the international ice core community in Switzerland.
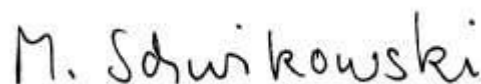
Margit Schwikowski

VOCATIONAL TRAINING: ACTINOMETRY METHOD DEVELOPMENT

C. Blétry (PSI), Y. Manoharan (PSI & ETHZ), D. Salionov (PSI LBK & EPFL), T. Hullar,
C. Anastasio (UCD), T. Bartels-Rausch (PSI)

With two experiments we optimized and characterized actinometry measurements. First, we determined the decay of the chemical actinometer in the dark. Second, we assessed the recovery.

During my third year as apprentice at PSI, I helped with actinometry experiments and got to know the entire procedure. With these measurements, one can determine how many photons per time hit a sample, for example in a flow tube. This is important for future and past experiments, in which we want to observe the decay of substances during light exposure over time.

This chemical actinometry relies on doping the samples with a chemical actinometer, exposing the sample to light, extracting the actinometer quantitatively from the sample holder, and measuring its concentration. The aim of the first experiment was to check if we wash the chemical actinometer completely from our sample holder.

The sample was prepared as follows. 100 µL stock solution of 2-nitrobenzaldehyde (2-NB, 2000 µM), which is our actinometer, was pipetted into a glass tube. The tube was then constantly turned while putting it into a cooled reactor until a thin ice film froze. A few seconds after it freezing, the tube was removed and placed in a beaker. The ice film was then melted by holding the tube vertically above the beaker and rinsed 6 times with 250 µL of acetonitrile (in total 1500 µL). For each cleaning step the tube was hold over a new beaker and rinsed. These solutions were then pipetted into HPLC vials. For each washing step one vial was used. Then, every sample was diluted with 750 µl acetonitrile, well mixed, and measured using LC-MS.
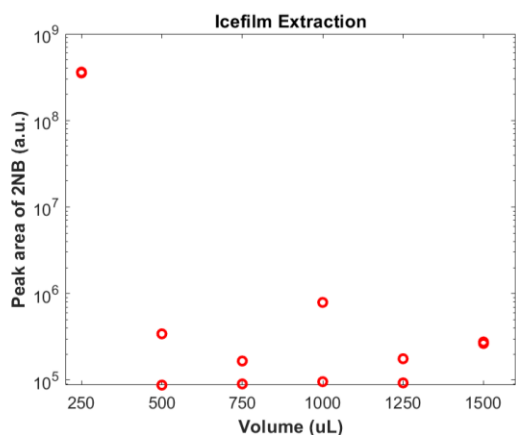
Fig. 1: Amount of 2-NB after each washing step.

Fig. 1 shows that the 2-NB was completely washed off in the first cleaning step. Only neglectable amounts of 2-NB appear to be left in the tube. Further quantification is ongoing. This result shows that the overall procedure can be optimized by minimizing the amount of acetonitrile to 250 µl in total.

The aim of the second experiment was a background measurement. This was achieved through executing the normal procedure but leaving a cover around the reactor to shield the tubes from the light. 100 µL stock solution of 2-NB (2000 µM) was pipetted into a glass tube. The tube was constantly turned while putting it into a cooled reactor until a thin ice film froze. This was done with 6 glass tubes.

Normally the cover would be removed at this point to let the lamps shine on the samples. We left the samples in the dark, and continued as usual. The timer was started, and every 30 seconds a glass tube was removed and placed into a separate beaker. The ice film was then melted by holding the glass tube vertically above a beaker, and rinsed 3 times with 500 µL of acetonitrile (in total 1500 µL). Each solution was then pipetted into a HPLC vial and analyzed using LC-MS.
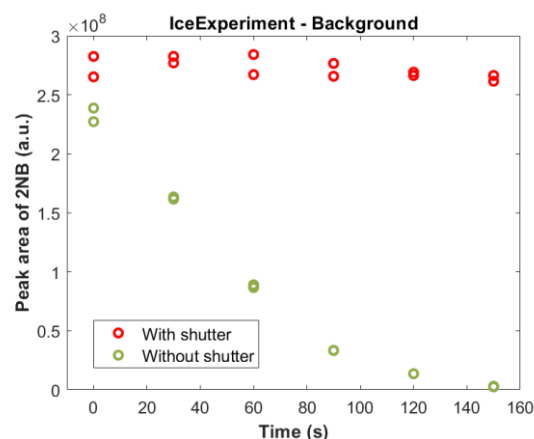
Fig. 2: Evolution of 2-NB over time. Once with and once without the irradiation of light.

In Fig. 2 we can clearly see the reduction of 2-NB when no shutter is used (green dots). After 150 seconds, all of it decayed. If the light is blocked with a cover, the 2-NB does not significantly decay (red dots). A slight loss over time can be seen. This background can now be subtracted from the measurements to correct these.

Overall, we are very satisfied with the results of both experiments. We will continue with actinometry measurements in the future.

---

[1] E. S. Galbavy et al., J. Photochem. Photobiol., **209**, 186-192 (2010).

HOW MUCH IRRADIATION REACHES OUR ICE SAMPLES?

Y. Manoharan (PSI & ETHZ), D. Salionov (PSI LBK & EPFL), T. Hullar, C. Anastasio (UCD), M. Ammann,
T. Bartels-Rausch (PSI)

We report the development of a chemical actinometry method for measuring the intensity of light in ice films in coated-wall flow-tube (CWFT) experiments, which is an important calibration step since photochemical reactions depend on the intensity of light for absorption [1].

The actinic flux is the total intensity of light available for a molecule for absorption, including direct, scattered and reflected radiation coming from all directions. Especially in ice films, the available light intensity for absorption can differ significantly from that hitting the reactor [2] and this variation can lead to inconsistencies when performing photolytic experiments. Here, we describe a method for determining the actinic flux directly in ice film samples in flow tubes.

Chemical actinometry uses the rate of photolytic decay of a species, in our case 2-Nitrobenzaldehyde (2-NB) to calculate the photon flux that was available for this species for photolysis [2]. Fig. 1 depicts the set-up of the coated-wall flow-tube experiments.
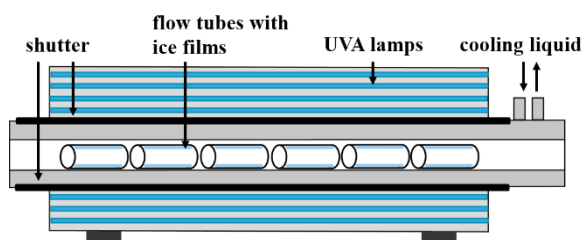
Fig. 1: Set-up of the CWFT experiments, with six short tubes coated inside with ice films and placed inside the cooled glass reactor, surrounded by seven UVA lamps for irradiation. The black cover to shield the flow tubes from the light before starting the experiment, is indicated as « shutter ».

Since we need a measurement of the decay of 2-NB in the ice film over time, six short glass tubes, aligned next to each other as depicted in Fig. 1, are used. Every 30 s, one of the tubes is removed, its ice film melted and collected for the later detection of the 2-NB concentration using HPLC with UV detection. Another new installation is the so-called "shutter", a black textile cover to shield the ice films from the light and that can be installed around the glass reactor. This cover was left in place, while the lamps were warming up and then quickly removed to start photolysis. This was essential in order to avoid 2-NB decaying before starting the experiment. A set of measurements were performed with UVA lamps of two different brands and four repetitions each to check if we get reproducible data. Fig. 2 shows the results of the actinic flux measurements.
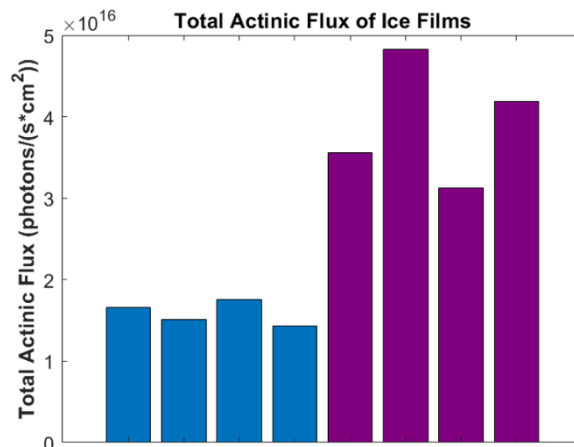
Fig. 2: Total actinic flux in ice films, of the UVA lamps brand Isolde (purple), and of the UVA lamps brand Philips (blue), and four repetitions each illustrated as individual bars.

The ice films, irradiated with Philips lamps, obtain an actinic flux of 1.6×10^{16} photons/(s·cm^2), and when irradiated with Isolde lamps an actinic flux of 3.6×10^{16} photons/(s·cm^2). These numbers are in excellent agreement with the actinic flux obtained when using NO$_2$ gas instead of 2-NB as a chemical actinometer, which is 1.6×10^{16} photons/(s·cm^2) when irradiated with Philips lams, and 4.3×10^{16} photons/(s·cm^2) with Isolde lamps. This might indicate, that scattering by the ice film and light absorption by the cooling liquid is negligible, or compensates. The standard error of 9.5% (Isolde lamps) was reduced to 4.6% by installing an improved shutter (Philips lamps).

Overall, we developed and optimized a method to apply chemical actinometry to our coated-wall flow-tube experiments. It gives us reproducible results for the actinic flux in our ice films, which serves as an important calibration to compare between different ice experiments but also to compare with other studies.

---

[1] T. Bartels-Rausch et al., Atmos. Environ., **44**, 5443-5450 (2010).
[2] E. S. Galbavy et al., J. Photochem. Photobiol., **209**, 186-192 (2010).

IRON(III) CITRATE PHOTOCHEMISTRY INDUCES IODATE REDUCTION

L. Iezzi (PSI & ETHZ), M. Reza (CUB, PSI), H. Finkenzeller (CUB), A. Roose (PSI & PhLAM),
T. Bartels-Rausch (PSI), R. Volkamer (CUB, PSI, ETHZ), M. Ammann (PSI)

Understanding the iodine cycle is a main topic in tropospheric chemistry. Here we show that iron(III) carboxylate photochemistry can have a role in the activation and recycling of iodate.

Iodine is of primary importance due to its influence on the oxidising capacity and the radiative balance of the atmosphere. Nevertheless there is still a lack of kinetic data and missing information on reactive iodine precursor gas fluxes [1]. Recently the measurements in the UTLS of Koenig et al. 2020 [2] have shown the persistence of IO in the gas-phase, and of both iodate (IO_3^-) and iodide (I^-) in particles, which is indicative of active recycling between the gas and particle phases, which may be driven by still not well understood iodate reduction processes. Iron(III)-carboxylate complexes are well known photoactive compounds, which can generate reactive oxygen species (ROS), such as HO_2 and H_2O_2 [3]. Previous work of this group demonstrated the link between carbonyl compounds, ROS and iodine chemistry [4], but the role of transition metals in the redox chemistry of iodine has not yet been clarified. Here, we suggest that iron(III) carboxylate photochemistry may play a role in the activation and recycling of iodine species. Thus, in this work we aim at investigating the reduction of iodate by H_2O_2 according to the Bray-Liebhafsky mechanism [5], where H_2O_2 would be provided by iron(III) carboxylate photochemistry.

We performed coated wall flow tube (CWFT) experiments with aqueous films of iodate and Fe(III) citrate (fe-cit) using citric acid (CA) as a matrix, which is an established proxy for oxygenated atmospheric organic matter and exhibits well characterized microphysical properties [6, 7]. The CWFT was coupled with a cavity enhanced differential optical absorption (CE-DOAS) instrument, provided by CU Boulder, in order to detect I_2 resulting from iodate reduction [8].

The plot of Fig. 1 illustrates the formation of $I_2(g)$ upon irradiation with UV-A and visible light. The results indicate that for both experiments fe-cit photochemistry promotes efficient iodate reduction. Furthermore the time profile suggests a complex reductive mechanism implying several chemical regimes where different contributions prevail according to the photochemical turnover of fe-cit and to the depletion of iodate as iodine reservoir. In fact the initial peak can be attributed to the complete photolysis of fe-cit, which leads to high amounts of ROS. This peak is narrower and higher under UV than in the visible, consistent with higher cross-section and thus higher photolysis rates of fe-cit in the UV than in the visible. Subsequently the photocatalytic cycle takes over continuously providing free radicals [6], which is consistent with $CO_2(g)$ measurements (not shown), but the resulting $I_2(g)$ may be consumed by

other competitive processes. It is notable that persistent longterm $I_2(g)$ production occurs that is higher under visible irradiation inspite of photolysis of $I_2(g)$ expected to be more significant in the visible. In turn, under UV-A, photolysis of an intermediate species or the formation of other products could occur (see Volkamer et al.).
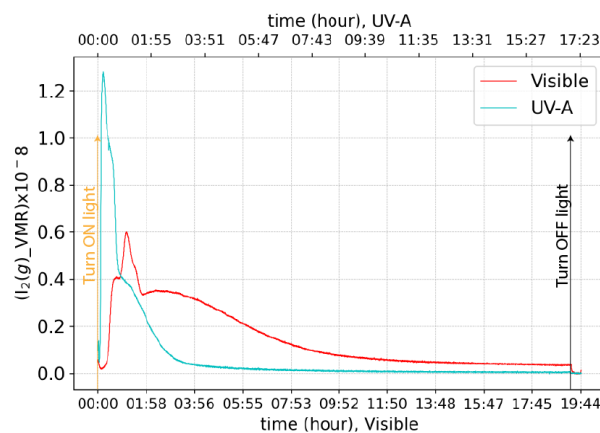
Fig. 1: Volume mixing ratio (VMR) values of I_2 (g) measured with CE-DOAS during CWFT experiments using visible (red line) or UV-A (blue line) light. Both experiments were performed at about 80% relative humidity using a coated film of 17.8 mg.

In conclusion, model and further experimental studies need to be carried out in order to interpret the experimental observations. This will aid at better understanding the recycling and activation of iodine species in the atmosphere and further emphasize the key role of iron(III) carboxylate complexes in multiphase chemistry.

[1] A. Saiz-Lopez et al., Chem. Rev., **112**, 1773–1804 (2012).
[2] T. K. Koenig et al., Proc. Natl. Acad. Sci., **117**, 1860-1866 (2020).
[3] L. Deguillaume et al., Chem. Rev., **105**, 3388-3431 (2005).
[4] P. Corral Arroyo et al., Atm. Chem. Phys., **19**, 10817-10828 (2019).
[5] L. Kolar-Anić and G. Schmitz, J. Chem. Soc. Faraday Trans., **88**, 2343-2349 (1992).
[6] J. Dou et al., Atmos. Chem. Phys., **21**, 315-338 (2021).
[7] D. M. Lienhard et al., J. Phys. Chem. A, **116**, 9954-9968 (2012).
[8] R. Thalman et al., J. Quant. Spectr. Rad. Tran., **147**, 171-177 (2014).

REDUCTION OF IODATE IN AQUEOUS ORGANIC AND INORGANIC THIN FILMS

M. Reza (CUB, PSI), L. Iezzi (PSI & ETHZ), H. Finkenzeller (CUB), A. Roose (PSI & PhLAM), T. Bartels-Rausch, M. Ammann (PSI), R. Volkamer (CUB, PSI, ETHZ)

The detection of iodine species in aged stratospheric air suggests the existence of recycling mechanisms reducing particulate iodate (IO_3^-) to form gas-phase iodine (I_2). We explore such processes in coated wall flow tube (CWFT) experiments.

Gas-phase IO radical and particulate IO_3^- have been observed to coexist in the stratosphere [1]. These observations, along with the recent discovery that iodine is released from dust in the free troposphere [2], highlight the need to better understand iodate recycling as a missing component of iodine chemistry as represented in atmospheric models. Iodic acid (HIO_3) efficiently forms particles, is a source of iodate [3], and forms by destroying ozone. Iodate reduction thus fuels a catalytic reaction cycle with implications for ozone destruction and new particle formation (NPF).

A quartz glass tube was coated with an aqueous solution containing sodium iodate and a matrix (i.e., either ammonium bisulfate (ABS), 1,2,3,4-butanetetracarboxylic acid (BTCA), citric acid (CA), or Fe(III) citrate (Fe-Cit) and CA) at a concentration ratio iodate:matrix = 1:100. A thin aqueous film forms on the inside walls by passing a stream of humidified air through the CWFT (~80% RH). For each film, three types of flow tube experiments were performed: (1) dark reaction with H_2O_2 involved flowing H_2O_2 through the CWFT for several hours in the dark; (2) photochemical experiments involved irradiating the CWFT with visible lights and UVA lights, separately; and (3) dark-aging experiments involved flowing H_2O_2 through the CWFT for several hours in the dark, followed by irradiation with visible light.

The formation of gas-phase I_2 from the aqueous films was measured by cavity enhanced differential optical absorption spectroscopy (CE-DOAS) coupled to the CWFT. Two custom (green and blue) CE-DOAS instruments were brought from Boulder to PSI. In addition to the CWFT experiments, trough reactor and other calibration experiments were conducted, and the PSI group was trained in the use of the CE-DOAS technique. Fig. 1 summarizes the preliminary results using the green CE-DOAS instrument in CWFT experiments. The I_2 released from aged films irradiated with visible light (type 3 experiments) was substantially greater to that from irradiated fresh films (type 2), or fresh films exposed to H_2O_2 in the dark (type 1). This increase of I_2 in inorganic and organic matrices suggests that a chromophore is formed from the reaction of iodate with H_2O_2.

Further experiments used Arizona Test Dust (ATD) and hematite (Fe_2O_3) in photochemical-dust experiments, not shown here, and confirm that dust chromophores also act as photosensitizers to enhance the rate of iodate reduction to I_2.

A photochemical pathway was discovered in which visible light is sufficient for reducing iodate to I_2, and the effect is more pronounced after the exposure of iodate to H_2O_2. This photochemistry is relevant in the atmosphere but not yet described in the literature. Further analysis is needed to determine the fractional yield of I_2 gas from iodate, as well as the reaction rate for the photochemical reduction of iodate. Integration of this process in atmospheric models would serve to better inform the iodine budget of an area of study, would aid in understanding diurnal trends of iodine species along with their impact on ozone destruction and new particle formation events.
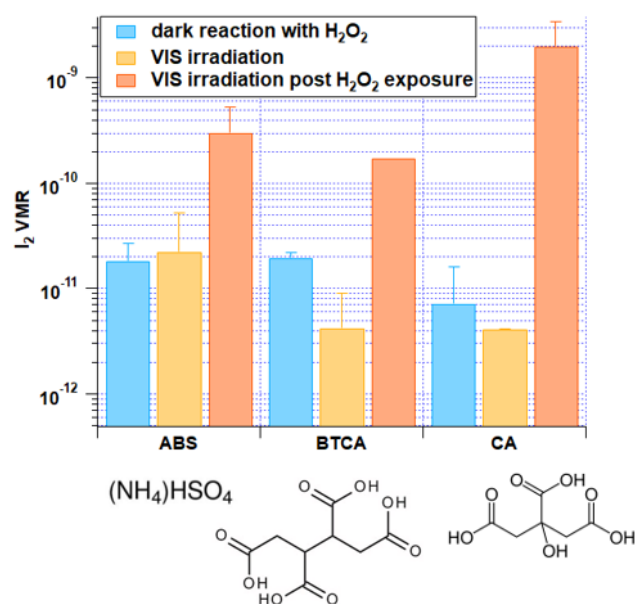
Fig. 1: I_2 (given as volume mixing ratio, VMR) produced from irradiated films aged with H_2O_2 (red) is greatly enhanced compared to dark (blue) and photochemical (orange) control experiments using fresh films.

[1] T. K. Koenig et al., PNAS, **117**, 1860-1866 (2020).
[2] T. K. Koenig et al., Sci. Adv., **7**, eabj6544 (2021).
[3] X. C. He et al., Science, **371**, 589-595 (2021).

IODINE CHEMISTRY: VOLATILE PRODUCTS MEASURED BY CIMS AND CE-DOAS

R. Volkamer (CUB, PSI, ETHZ), P. Sardana, R. L. Mauldin, H. Finkenzeller, M. Reza (CUB, PSI), A. Roose (PSI),
L. Iezzi (PSI & ETHZ), T. Bartels-Rausch, M. Ammann (PSI)

Atmospheric iodine forms particles by adding iodate (IO_3^-), but the fate of IO_3^- (and I^-) in particles is uncertain. We explore the chemical diversity of volatile organic-, inorganic- and iodo-organic products of multiphase recycling chemistry.

Iodine emissions from oceans have tripled since 1950, largely due to increased deposition of hemispheric pollution ozone into surface oceans. This anthropogenically stimulated source of naturally occurring iodine nowadays affects the stratospheric ozone layer [1]. The co-existence of iodine oxide (IO) radicals in the gas phase and particulate IO_3^- in stratospheric air, and evidence for aeolian iodine sources from dust aerosol suggest IO_3^- reduction is widely operative in the atmosphere [1,2]. However, atmospheric models do not widely consider IO_3^- as a reactive intermediate of the iodine geochemical cycle. Better knowledge about IO_3^- reduction and I^- oxidation rates in aerosols is needed to better quantify iodine impacts in the atmosphere, i.e., as ozone sink, source of particles, and trace element that modifies the lifetime of climate active gases (e.g., O_3, CH_4) [3-4]. Moreover, little is known about the sources and identity of soluble organic iodine, present in fine (acidic) particles over oceans [5].

The University of Colorado Boulder (CUB) group is preparing a CI-API-LTOFMS (CIMS) instrument with interchangeable ion sources for aircraft measurements of condensable vapors (sulfur, iodine, organics) that nucleate and grow nanoparticles over Colorado, Hawaii, and Alaska in Spring 2022 (TI^{3}GER field campaign, "Technological Innovation Into Iodine for GV Environmental Research", NSF-AGS-2027252, PI: R. Volkamer). The CIMS instrument was brought to PSI, and together with two CE-DOAS instruments was coupled to the photochemical coated wall flow tube (CWFT, see Reza et al.; Iezzi et al.) and a trough reactor (Roose et al.) to calibrate CIMS using CE-DOAS, optimize reagent ions (Br^-, I^-) by adding acetonitrile to suppress water clusters, and assess ozone sensitivities. A training dataset was generated that characterizes capabilities to measure oxygenated volatile organic compounds (OVOC), iodo-OVOC (I-OVOC), and inorganic iodine species. Comparison to accurate CE-DOAS I_2 measurements was used to demonstrate the sensitivity and linearity of the CIMS measurements.

Fig. 1 shows selected CIMS products formed in the CWFT experiments upon irradiation of an aqueous organic film containing a photosensitizer and iodate (iodate:Fe-citrate:citric acid = 1:10:100; 80% relative humidity) with visible light in the absence of ozone. Three classes of products were detected: a) inorganic iodine species (red): $I_2 \cdot I^-$ (m/z 269.804, major signal), $HOI \cdot I^-$ (m/z 270.812, minor), $I \cdot I^-$ (m/z 253.809, minor) and

$IO \cdot I^-$ (m/z 269.804, minor). All time variations were similar to I_2. Experiments are planned to characterize I_2 fragmentation in the absence of free radicals. b) OVOC (green): $C_4H_6O_3 \cdot I^-$ (m/z 228.936, major), a plausible product of citric acid decarboxylation, increased steadily after visible lights were turned ON. c) I-OVOC (blue): $C_3H_4OI_2 \cdot I^-$ (m/z 436.740, moderate), $C_3H_3OI_3 \cdot I^-$ (m/z 562.636, moderate), $C_4H_5O_3I \cdot I^-$ (m/z 354.833, minor), $CHI_3 \cdot I^-$ (m/z 520.626, minor), $C_2H_2O_4I_2 \cdot I^-$ (m/z 470.709, trace), exhibited temporal variations consistent with first and higher generation products.
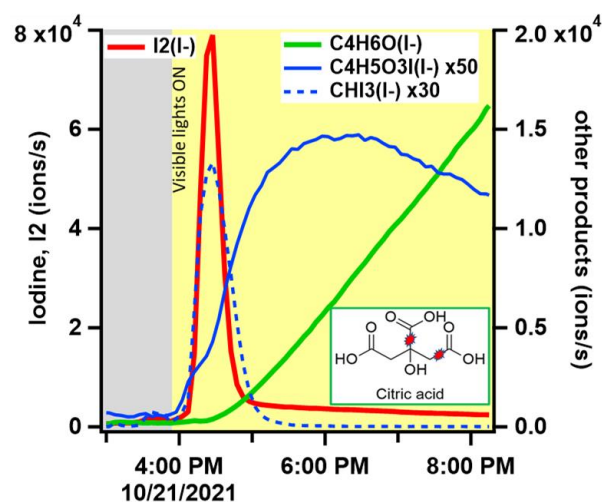
Fig. 1: Time series of volatile products that evaporate from the aqueous organic film irradiated with visible light, mostly as I_2 (red, left), and also as OVOC fragments of citric acid (green, right) and mono-, di- (not shown), and tri-iodo-OVOC (blue, right).

Additional CWFT experiments were conducted in the absence of IO_3^-, and hold potential to test and develop models of Fe-Cit photochemistry. Dark experiments involved flowing H_2O_2 over IO_3^-/citric acid films, and exposing I^- solutions to ozone in the trough reactor.

---

[1] T. K. Koenig et al., PNAS, **117**, 1860-1866 (2020).
[2] T. K. Koenig et al., Sci. Adv. **7**, eabj6544 (2021).
[3] X. C. He et al., Science, **371**, 589-595 (2021).
[4] X. Wang et al., Atmos. Chem. Phys., **21**, 13973-13996 (2021).
[5] A. R. Baker and C. Yodle, Atmos. Chem. Phys., **21**, 13067-13076 (2021).

IODIDE OXIDATION BY OZONE: A PATHWAY TO IO AND I_2

A. Roose (PSI), S. Gysin (PSI & ETHZ), H. Finkenzeller (CUB), R. Volkamer (CUB, PSI, ETHZ), M. Ammann (PSI)

Recent aircraft measurements report significant amounts of inorganic iodine in the lower stratosphere possibly representing a sink for ozone. Here, we study the formation of I_2 and IO from the reaction of ozone with iodide.

Tropospheric multiphase redox reactions lead to gas phase iodine species as well as both oxidized (iodate) and reduced (iodide) particulate iodine in the lower stratosphere [1]. This may influence stratospheric ozone depletion as iodide can directly destroy ozone (O_3) through reaction in the bulk aqueous phase or at interfaces [2,3]. The temperature dependence of this reaction is only poorly constrained.

Sakamoto et al. [4] have studied this reaction and provided first evidence for IO formation, with 4 main features observed: (1) $I_2(g)$ and IO(g) are released ([$I_2(g)$] > 100[IO(g)]) during the reaction of $O_3(g)$ with KI(aq). (2) IO(g) yields are independent of bulk pH between 2 and 11, whereas $I_2(g)$ production is markedly enhanced at pH < 4. (3) $I_2(g)$ and IO(g) produced are directly proportional to [KI(aq)] up to 5 mM.
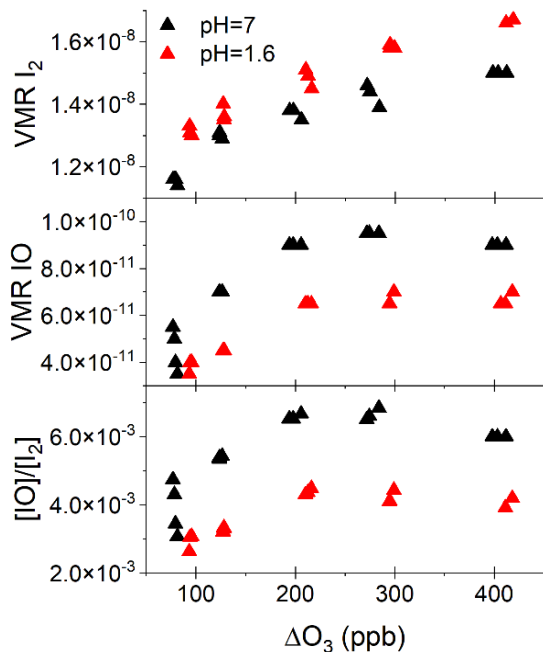
Fig. 1: Preliminary volume mixing ratio (VMR) of I_2, IO and IO/I_2 ratio versus the consumed ozone mixing ratio at [I^-] = 5.10^{-4} M in pure water, T = 283.15K, and different pH.

We measured the loss of O_3 to aqueous iodide solutions in a trough reactor described by Artiglia et al. [5] (for bromide). Cavity enhanced differential optical absorption spectroscopy [6,7] coupled to the trough reactor has allowed monitoring gas phase I_2 (508–554 nm range) and IO radical (420–490 nm range).

Fig. 1 and Fig. 2 show preliminary results for iodide solutions in pure water. While I_2 formation is increasing with increasing ozone consumption, formation of IO radicals reached a plateau indicating its formation is related to a surface-dependent mechanism. According to Fig. 1, the lowering of the pH clearly increases the I_2 mixing ratio as observed by Sakamoto et al. [4], likely due to the acid catalysis of the reaction of HOI with I^-. However the IO radical yield is lower at lower pH, requiring further investigation.

As shown in the lower panel of Fig. 1 and Fig. 2, the saturating IO production leads to a maximum of the [IO]/[I_2] ratio, because I_2 formation continues to increase. The position of the maximum as a function of the consumed O_3 indicates a dependency on the temperature.
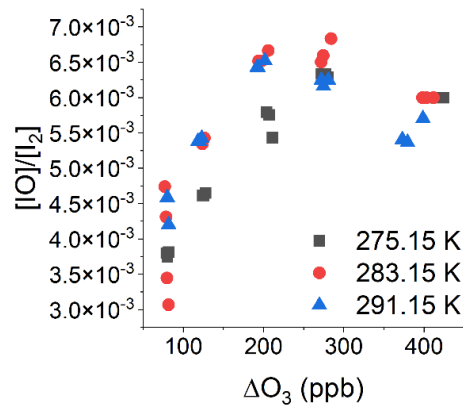
Fig. 2: Preliminary IO/I_2 ratio as a function of the consumed ozone concentration at [I^-] = 5.10^{-4} M at pH = 7 in pure water and at different temperature.

[1] T. K. Koenig et al., PNAS, **117**, 1860-1866 (2020).

[2] L. J. Carpenter et al., Nat. Geosci., **6**, 108–111 (2013).

[3] Y. Sakamoto et al., J. Phys. Chem. A, **113**, 7707–7713 (2009).

[4] C. Moreno et al., Phys. Chem. Chem. Phys., **22**, 5625-5637 (2020).

[5] L. Artiglia et al., Nat. Commun., **8**, art. no. 700 (2017).

[6] M. Wang et al., Atmos. Meas. Tech., **14**, 6955–6972 (2021).

[7] R. Thalman and R. Volkamer, Atmos. Meas. Tech., **3**, 1797–1814 (2010).

RADICALS PRODUCED OR DESTROYED?

P. A. Alpert (PSI), K. Kilchhofer (PSI & ETHZ), K. Y. Cheung, R. L. Modini (PSI LAC), L. Torrent,
C. Ludwig (PSI LBK), M. Ammann (PSI)

The dominant reaction pathways and rates in aerosol particles composed of organic-metal complexes were investigated using X-ray spectromicroscopy in this study coupling iron and copper cross-reactions.

Aerosol particles composed of organic-metal complexes generate a significant amount of radicals as the result of photochemical reactions and cycling of metal oxidation states. Reactive species generated in our lungs are hazardous to our health, and are the result of being exposed to particles laden with metals, such as Cu and Fe [1]. In a recent study, Cu and Fe were shown to be responsible for $70 - 90\%$ of total radical production when tested in epithelial lung lining fluid, and the remaining $10 - 30\%$ was attributed to chemical reaction involving O_3, NO_2, and secondary organic aerosol (SOA) particles [2]. Although, previous work has shown catalytic radical destruction in aerosol particles due to cross redox reaction, $Cu^+ + Fe^{3+} \rightarrow Cu^{2+} + Fe^{2+}$ followed by fast reactions of Cu^{2+} or Fe^{2+} with radicals [3]. Therefore, detailed information on radical production and determining metal oxidation state changes during cycles should result in better quantitative understanding of radical chemistry in atmospheric aerosol particles.

We report a in situ X-ray spectromicroscopic study of single particles composed of citric acid, iron(III)-citrate and copper(II)-citrate (mole ratio is 5:5:1) exposed to UV light in a humidified environmental cell. The iron(III) fraction, β, was quantified during chemical and photochemical reactions inside single particles [46]. Particles were nebulized, dried and deposited by impaction into the cell mounted in the scanning transmission X-ray microscope at the PolLux end station of the Swiss Light Source. Under controlled relative humidity of 45%, pressure at 150 mbar, and O_2 partial pressure of 40 mbar, particles were illuminated with UV light (Lux-iGen^{TM} 365nm UV LED) using a fiber optic coupling. During oxidation, we imaged particles resulting in finely detailed maps of β, which were then converted to 2-D column integrated pixelated profiles.

Fig. 1 shows that UV light reduced β, where the grey and colored symbols are values of β prior to irradiation and after the light was switched off, respectively. In the first few minutes of re-oxidation (dark blue symbols), β was about 0.3 toward the center of particles, i.e. > 10 pixels from the perimeter. Near the perimeter, β amazingly was already close to initial values. This exactly means there was significant O_2 availability and radical production to re-oxidize Fe^{2+} on similar time scales as the photochemical reaction rate. The slopes β indicate gradients through the particles, which were expected as the particles were highly viscous and limiting the diffusive transport of O_2 and metals (as ions or in complex

with organic molecules). In turn, the lack of fast reoxidation in the particle interior also means that O_2 should be much less available there to react with carbon centered radicals (CCRs) and form smaller reactive oxygen species (ROS), such as HO_2. From these results, we can conclude that radicals instead persisted inside particles. We argue that reactions involving O_2, Cu-Fe cross reactions and diffusion limitations all need to be considered to explain favored ROS production pathways near the surface and CCR persistence in the interior in aerosol particles.
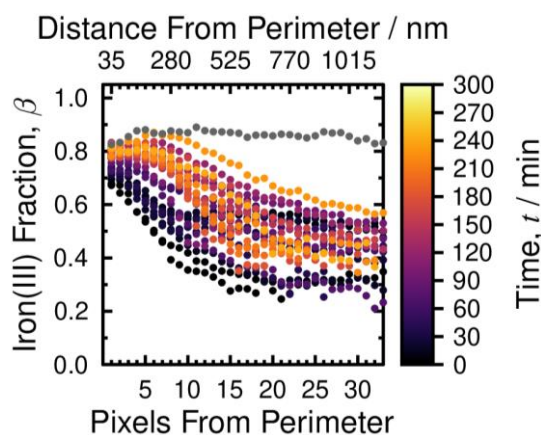
Fig. 1: A profile of β in aerosol particles after being reduced by UV exposure for 10 min and then oxidized in situ in the dark. The light was switched off at $t = 0$ min and the color indicates the time that X-ray spectromicroscopic images were acquired. The bottom abscissa are concentric pixels from the perimeter of the 2-D imaged particles, where a value of 1 is the perimeter pixels. The top abscissa corresponds to our pixel size of 35×35 nm^2.

[1] A. Tapparo et al., Chemosphere, **241**, art.no. 125025 (2020).
[2] S. Lelieveld et al., Environ. Sci. Technol., **55**, 14069-14079 (2021).
[3] J. Mao et al., Atmos. Chem. Phys., **13**, 509-519 (2013).
[4] J. Dou et al., Atmos. Chem. Phys., **21**, 315-338 (2021).
[5] P. A. Alpert et al., Nat. Commun., **12**, art. no. 1769 (2021).
[6] P. A. Alpert et al., Phys. Chem. Chem. Phys., **21**, 20613-20627 (2019).

UV LIGHT AGES METAL CONTAINING ORGANIC AEROSOLS

K. Kilchhofer (PSI & ETHZ), D. Bell, M. Surdu, I. El Haddad (PSI LAC), M. Ammann (PSI)

We present the detection of photochemically produced organic compounds in transition metal containing organic aerosol with an EESI-TOF-MS. This method enables us to directly follow the organic composition at changing ambient conditions.

Chemical aging of atmospheric particles triggered by photolysis of transition metal complexes in organic aerosol (OA) alters radical chemistry and thus generates reactive species causing oxidative stress in the lung [1, 2]. Complexation of metals such as iron and copper in OA particles can occur via coalescence of existing OA with solid dust particles followed by dissolution of the metals. Aqueous aerosol particles prevail in very different phase-states depending on humidity, and hence, diffusion rates of e.g. O_2 or other reactants change. We previously suggested that the formation of peroxy radicals consumes all O_2 in viscous OA degradation induced by Fe-carboxylate photolysis [1]. In highly-viscous conditions, radical-radical recombination is diffusion limited, which slows aerosol decomposition and favors other product pathways. We measured the different products from Fe-citrate (Fe-cit) containing citric acid (CA) aerosol at varying O_2 partial pressure and humidity by making use of an extractive electrospray ionization time of flight mass spectrometer (EESI-TOF-MS, [3]). CA was used as a proxy for oxygenated OA with well known microphysical properties. In parallel, we are investigating the influence of copper in this model system.
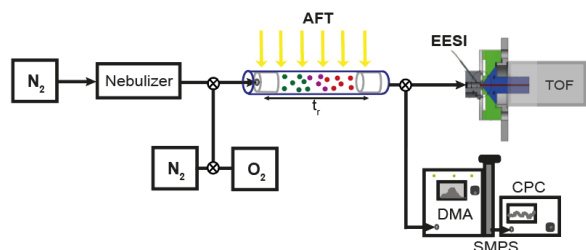
Fig. 1: Aerosol flow tube setup coupled to an EESI-TOF-MS and SMPS system.

The experiments were conducted with an aerosol flow tube (AFT) as schematically shown in Fig. 1. The photochemical aging process was mimicked with UV-lamps surrounding the AFT, and we have built a flow system so that humidity and carrier gas composition are variable. The aerosol mass concentration was monitored with an SMPS system and the automatic valve switching between HEPA filter and aerosol signal was used for background subtracting the MS time series. In a first campaign, we assessed the influence of different mole ratios of the iron/copper citrate/CA particles on their photochemical behavior. A time series of a major fragmentation product ($C_5H_6O_5$) upon photolysis of the iron citrate complex is shown in Fig. 2 during two irradiation periods at different environmental conditions. The TOF-MS signal increase during irradiation periods confirms the light-induced formation of that product. Moreover, the signal intensity varied with changing humidity, oxygen partial pressure and iron/copper ratio. This will lead to valuable conclusions whether the carbon-centered free radical formed after decarboxylation of the acid group near the alcohol group react with oxygen to lead to the oxidation of the alcohol group, thus the ketodicarboxylic acid observed, or rather undergoes radical – radical recombination.
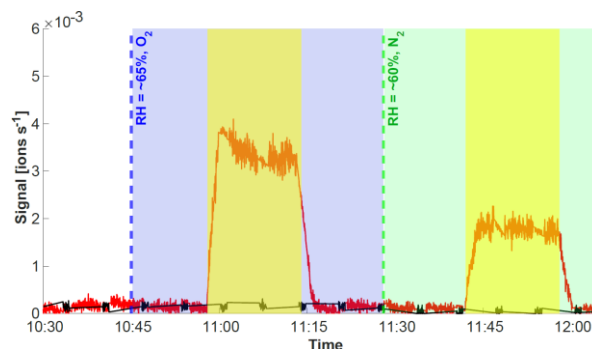
Fig. 2: Time series of the photochemical fragmentation product, a ketodicarboxylic acid ($C_5H_6O_5$, red), of an iron citrate/CA 1:10 experiment. The yellow area represents times of irradiation and the vertical-dashed lines separate carrier gas conditions (blue vs. green).

The photochemical yield of other organic products need to be further evaluated towards their exact molecular composition. This could be resolved in experiments with an ultrahigh-resolution MS (EESI-Orbitrap [4]). Yields of all products formed under light will be used to assess the evolution of different aerosol composition at changing conditions. In the meantime, we are running experiments to assess the kinetics of the formation of these products, by varying the residence time in the AFT. The findings will help to understand the turnover of free radicals and chemical aging in OA particles experiencing different metal contents, phase-states and thus, oxygen supply.

---

[1] P. A. Alpert et al., Nat. Commun., **12**, art. no. 1769 (2021).

[2] J. Dou et al., Atmos. Chem. Phys., **21**, 315-338 (2021).

[3] F. D. Lopez-Hilfiker et al., Atmos. Meas. Tech., **12**, 4867–4886 (2019).

[4] C. Ping Lee et al., Env. Sci. Technol., **54**, 3871−3880 (2020).

XPS INVESTIGATION OF FERRIC ORGANIC COMPLEXES

L. Artiglia (PSI LSK & LUC), L. Iezzi (PSI & ETHZ), A. Roose (PSI), K. Raj, H. Mohammadjafari Sadeghi,
N. L. Prisle (ATMOS), M. Ammann (PSI)

This work shows the characterization of aqueous solutions containing ferric organic complexes by means of liquid jet x-ray photoelectron spectroscopy and resonant photoemission.

In previous years, we carried out a complete investigation of ferrous and ferric sulfate aqueous solutions interfaces by means of ambient pressure X-ray photoelectron spectroscopy (APXPS), near edge X-ray absorption fine structure (NEXAFS) spectroscopy and resonant photoemission (RPES). Such studies allowed to identify the structure and spin of the aquo-complexes, and to exclude strong hybridization between iron and water molecules. Furthermore, with the help of molecular dynamics simulations, the presence of partially complexed ions at the liquid-vapor interface has been ruled out. Based on XPS results, the reaction of ferrous ions with hydrogen peroxide, also known as Fenton's reaction, leads to iron oxidation and the production of hydroxyl radicals (Haber-Weiss mechanism) [1]. This is in agreement with the literature, which showed that non-complexed or partially-complexed ferrous ions are essential to favor the formation of highly-valent iron species (ferryls) [2], following the Bray-Gorin mechanism [3]. In summary, ferrous ions quickly form complete octahedral complexes with water, which are homogeneously distributed in the solution and, after the addition of hydrogen peroxide, lead to ferric ions and hydroxyl radicals. The use of organic ligands may alter the surface properties of iron, possibly enriching its amount at the liquid-vapor interface. Surface-enriched iron ions may show an incomplete coordination shell, thus favoring the Bray-Gorin mechanism. In this work, we investigated ferric organic complexes (citrate and oxalate). The main goal was to check the local amount of iron, in comparison to the sulfate aqueous solution. Experiments were performed at the X11MA (SIM) beamline at the Swiss light source synchrotron. 0.1 mol/L aqueous solutions were injected in vacuum by means of a liquid microjet (liquid filament diameter in the 25 μm range) and photoelectrons generated at the liquid-vapor interface were detected by means of a differentially pumped electron analyzer. RPES experiments were carried out scanning the valence band across the iron L_3 absorption edge.

Fig. 1a shows the Fe 2p spectra of 100 mM ferrous sulfate solution, and the same ions (same concentration) complexed with oxalate and citrate. The spectrum of 300 mM FeSO$_4$, acquired in a previous beamtime, is also plotted in Fig. 1a, as a reference for peak positions, shape and spin-orbit-splitting. The concentration of Fe^{3+} in this work was set to 100 mM due to the solubility in water of the complexes. None of the 100 mM solutions displays a definite signal, indicating that iron is

below the detection threshold (within the probing depth – 1.0 nm - of the technique at a kinetic energy of approximately 300 eV). Fig. 1b displays the C 1s peaks of oxalate and citrate anions. Both signals are detected: oxalate shows a single feature (ca. 294.0 eV), corresponding to the two carbons having the same oxidation state, whereas citrate shows carboxylic (ca. 294.5 eV), alcoholic (ca. 292.2. eV) and aliphatic (290.6 eV) features. RPES data in Fig. 1c, d and e show the spectra acquired off-resonance (hv=702 eV), close to the pre-edge (hv=706 and 708 eV) and at the absorption maximum (hv=710 eV). While in the case of ferric sulfate the resonance of Fe 3d orbitals (shoulder at ca. 9.5 eV) appears only at 710 eV, in the case of organic complexes a shoulder is detected also at 706 (708) eV, and its relative intensity at 710 eV seems larger. Such a behavior may suggest a larger accumulation of iron within the probing depth of the technique. Further data processing is required to confirm such findings.
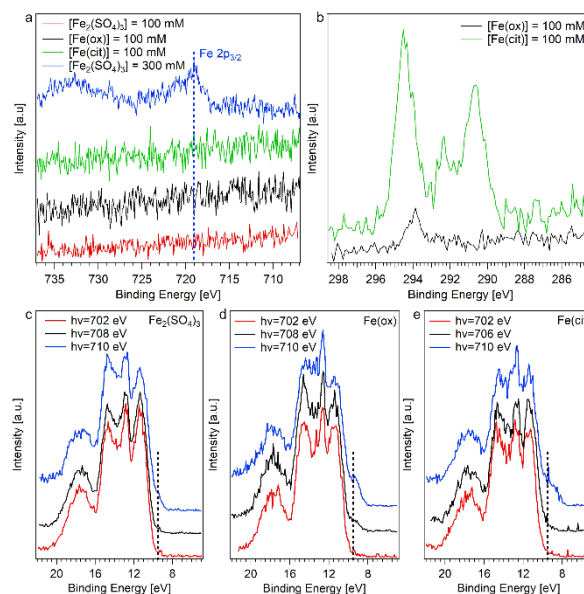
Fig. 1: (a,b) Photoemission spectra of Fe 2p and C 1s of the solutions investigated; (c,d,e) RPES across the Fe L_3 threshold.

[1] F. Haber, J. Weiss, Proc. Roy. Soc. A., **134**, 332-351 (1934).

[2] H. Sugimoto, D. T. Sawyer, J. Amer. Chem. Soc., **106**, 4283-4285 (1984).

[3] W. C. Bray, M. H. Gorin, J. Amer. Chem. Soc., **54**, 2124-2125 (1932).

INTERPLAY OF IONIC SURFACTANTS WITH BROMIDE IONS

R. Abouhaidar (PhLAM), S. Chen, H. Yang (PSI & ETHZ), L. Artiglia (PSI LSK & LUC),
C. Toubin (PhLAM), M. Ammann (PSI)

Surface active organics are important components in sea water and sea spray aerosol. Here, we use X-ray photoelectron spectroscopy and molecular dynamics simulations to assess the role of ionic surfactants on the abundance of bromide at interfaces.

Bromide ions are implicated in halogen activation processes relevant for the ozone budget in the troposphere. The abundance of bromide (Br⁻) ions, reaction intermediates and products at the aqueous solution – air interface is crucial in these processes [1, 2]. In turn, sea water is often containing surface active organic compounds, including ionic surfactants of both polarities. We have recently shown that tetrabutylammonium (TBA) leads to a strong enhancement of Br⁻ at the interface and to a related increase of the reactivity with ozone [3]. Here, we investigate both experimentally and theoretically the impact of the positively charged hexylammonium and the negatively charged propylsulfate on the abundance of Br⁻ anions and sodium (Na⁺) cations. Fig. 1, in the middle (black line), shows the photoemission (PE) spectrum of a 0.1 M NaBr aqueous solution obtained at 229 eV photon energy and featuring the spin-orbit split doublet of Br 3d5/2 and 3d3/2 of Br⁻ and the Na 2s peak of Na⁺. Upon addition of 0.1 M hexylamine (red, top) and mixed 0.1 M propylsulfate (blue, bottom) to the NaBr solution, the Br 3d PE intensity increases and decreases, respectively, clearly showing the impact of the electrostatic interactions caused by the headgroups of different polarity. The Na 2s shows the opposite behavior.

Fig. 2 shows preliminary molecular dynamics results of Br⁻ surface propensity as a function of the position with respect to the interface. Br⁻ is attracted to the interface, indicated by the yellow region, in presence of hexylamine or hexylammonium, as observed experimentally. Also, in presence of propyl sulfate, the relative Br⁻ density is consistently lower than in the pure NaBr case. Additional calculations are planned with higher concentrations to confirm this trend.
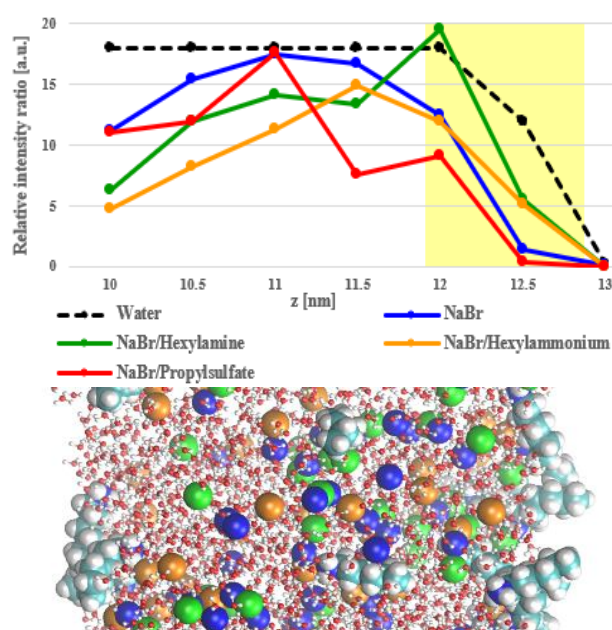
Fig. 2: Upper panel: surface propensity of Br⁻ for different solutions, expressed as relative Br⁻ density as a function of the distance perpendicular to the interface. The interfacial region is highlighted in yellow. Lower panel: molecular view of a hexylammonium bromide / NaCl solution. Color code for the ions: Br: orange, Cl: green, Na: blue, O: red, H: light grey, C: light blue.

[1] L. Artiglia et al., Nat. Comm., **8**, art. no. 700 (2017).
[2] I. Gladich et al., J. Phys. Chem. Lett., **11**, 3422-3429 (2020).
[3] S. Chen et al., ACS Earth Space Chem., **5**, 3008-3021 (2021).

Fig. 1: Br 3d and Na 2s PE spectra of 0.1 M aqueous NaBr (black, middle), with added 0.1 M hexylamine (red, top) or 0.1 M propylsulfate (blue, bottom), measured at 229 eV photon energy. Shadings indicate Gaussian peak fits.

HONO FROM IRON(III) COMPLEX PHOTOCHEMISTRY IN THE TROPOSPHERE

L. Iezzi (PSI & ETHZ), A. Tilgner, E. Hoffmann (TROPOS), M. Ammann (PSI), H. Herrmann (TROPOS)

Iron(III) carboxylate photochemistry can generate Reactive Oxygen Species (ROS). Here, we assess the tropospheric relevance of ROS for the conversion of NO$_2$ into HONO by using the explicit aqueous phase chemical box model CAPRAM.

Several studies have highlighted the importance of iron(III) carboxylate complexes in the troposphere as chromophores to initiate radical chemistry in aerosol particles involving ROS [1]. To date the formation mechanism of HONO in the atmosphere is still not completely understood and current research is focusing on photochemical processes involving heterogeneous conversion of NO$_2$(g) in aerosol particles [2, 3]. To assess the impact of Fe-carboxylate photochemistry on NO$_2$ conversion we used the explicit aqueous phase chemical box model CAPRAM [4]. Furthermore, in order to investigate atmospheric implications and the role of the aqueous phase we used the air parcel model SPACCIM which allows to investigate both cloud droplets and deliquesced particles according to the altitude where the air parcel is passing through. The multiphase chemistry mechanism of SPACCIM is comprised of the gas phase model MCMv3.2 and the aqueous phase CAPRAMv4.0 which further describes the phase transfer process implemented with the kinetic resistance model of Schwartz [5].

The first hypothesis has been that HO$_2$ resulting from Fe-carboxylate photochemistry can react with NO$_2$ leading to HONO through the formation of peroxynitric acid (HNO$_4$) [6, 7]. Hence, the scope of this work is to evaluate the importance of NO$_4^-$ decomposition on HONO formation by performing sensitivity studies and assessing chemical sources and sinks. Thus, several simulations were performed by changing the chemical mechanism of the model, the emission scenario, the iron content of the aerosol phase, the photolysis efficiency and the occurrence of cloud periods. Fig 1. illustrates the main findings of these simulations. We can observe that in an urban scenario the main source of HONO$_{(aq)}$ during a cloud period is the photolysis of NO$_3^-$ in the condensed phase which produces NO$_2^-$. However by removing the competitive reaction with sulfite the NO$_4^-$ pathway becomes the main source of NO$_2^-$ in the condensed phase. In the remote scenario the fluxes are generally lower, probably due to lower NO$_x$ concentrations, but the NO$_4^-$ pathway dominates the condensed phase chemistry even in presence of sulfite. Analyzing the sources and sinks of the remote scenario for NO$_4^-$ and NO$_{2(aq)}$ we observed the same results, especially for NO$_{2(aq)}$ where the reaction with superoxide is the main sink. Furthermore there is evidence that the condensed phase chemistry gains importance during cloud periods rather than during the aerosol period, where gas phase chemistry dominates.
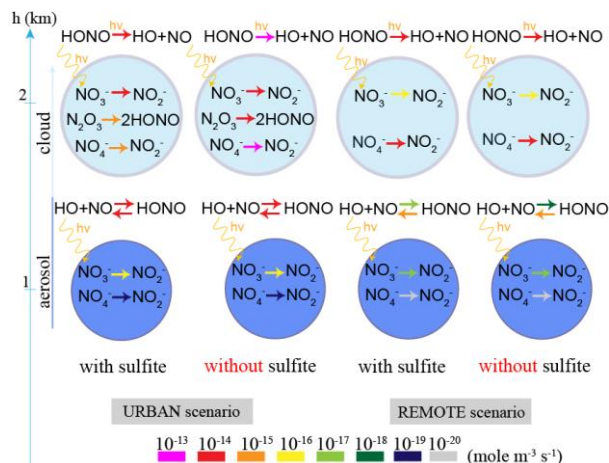
Fig. 1: Main chemical pathways for deliquesced particles and cloud droplets considering chemical mechanisms with and without the reaction between sulfite and HNO$_4$ in the condensed phase, applied for two different scenarios. The color of the arrows indicates the approximate average turnover (per volume of air) of the reactions, calculated for the second day of the simulation.

We can conclude that there is a clear impact of sulfur chemistry in suppressing the NO$_4^-$ pathway as a source of HONO. However, it may become important in a non-polluted scenario, where SO$_2$ levels are low. Finally increasing the iron content leads to lower HONO concentrations during cloud periods, even though in the urban scenario this can be observed only in absence of sulfite. More model studies are needed to shed light at this disclosure and adding experimental findings would help to better understand the role of iron(III) carboxylate photochemistry.

[1] L. Deguillaume et al., Chem. Rev., **105**, 3388-3431 (2005).

[2] F. Spataro and A. Ianniello, J. Air Waste Manage. Assoc., **64**, 1232-1250 (2014).

[3] X. Lu et al., Environ. Res. Lett., **13**, art. no. 114002 (2018).

[4] H. Herrmann et al., Atmos. Environ., **39**, 4351-4363 (2005).

[5] A. Tilgner et al., J. Atmos. Chem., **70**, 221-256 (2013).

[6] N.K. Scharko et al., Environ. Sci. Technol., **48**, 11991-12001 (2014).

[7] X. Wang et al., Environ. Sci. Technol. Lett., **8**, 53-59 (2020).

O:C DETERMINES NUMBER OF PHASES IN ORGANIC AEROSOL MIXTURES

F. Mahrt (PSI & UBC), Y. Huang, J. Zaks, A. Devi, L. Peng (UBC), P. E. Ohno, Y. Qin, S. T. Martin (Harvard),
M. Ammann (PSI), A. K. Bertram (UBC)

Atmospheric aerosol particles often contain primary organic aerosol (POA) and secondary organic aerosol (SOA) components. Here, we investigate the phase behavior, i.e., the number and types of phases, in mixtures of POA and SOA material.

Aerosol particles affect air pollution and climate. A large mass fraction of tropospheric aerosols is composed of organic aerosol (OA). OA is often categorized into primary organic aerosol (POA) and secondary organic aerosol (SOA) [1]. POA denotes particles that are directly emitted into the atmosphere. Hydrocarbon-like organic aerosol (HOA), with typical oxygen-to-carbon (O:C) ratio of $0.02 \leq$ O:C ≤ 0.26, denotes a main type of POA in urban environments. Examples of HOA are engine lubricating oils coming along with unburnt fuel components. By contrast, SOA is formed within the atmosphere, mostly through oxidation of volatile organic compounds (VOCs), followed by gas–particle partitioning of the reaction products. Precursors of SOA are emitted from both anthropogenic and biogenic emissions. Examples of biogenic emissions include α-pinene, limonene and β-caryophyllene, while toluene, catechol, xylene and cyclohexene are examples of anthropogenically emitted VOCs. The O:C ratio of ambient SOA material usually ranges from ~0.32 to 1.32. When HOA and SOA become internally mixed within individual aerosols, particles with either one or two phases can form. In order to predict the role of OA for air pollution and climate, knowledge on the phase behavior, i.e., the number and type of phases formed in such HOA+SOA particles is important, as the number of phases impacts many processes including heterogeneous chemistry, gas–particle partitioning and in turn particle growth and size distribution, ultimately affecting climate. If HOA + SOA are completely miscible the presence of HOA seed particles enhances the SOA formation, by providing additional OA mass for semivolatile organic compounds to partition into. In contrast, such an enhancement is absent, if internal mixtures form two distinct aerosol phases. We have previously shown that one- or two-phase particles can form when mixing single-component commercially available proxies of HOA and proxies of SOA [2]. Nevertheless, real atmospheric SOA is considerably more complex than the single-component SOA proxies used previously. Thus, studies with more realistic SOA are needed to confirm the conclusions from our recent study. Here, we have investigated the phase behavior of 11 HOA proxies with 7 different SOA materials, generated in environmental chambers, using fluorescence microscopy.

Fig. 1 shows exemplary microscopy images, for HOA + SOA mixtures taken at a relative humidity (RH) of 90%, revealing that particles with either one or two phases can form. We found that the phase behavior for our 77 unique HOA + SOA mixtures was independent of RH between 90% to 0% [3].
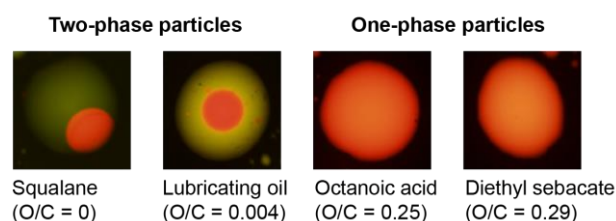
Fig. 1: Example fluorescence microscopy images of α-pinene SOA material mixed with HOA proxies of different O:C ratios. All images were taken at 90% RH.

Fig. 2 summarizes the number of phases as a function of the absolute difference in the average O:C ratio of the HOA and SOA components, i.e., ΔO:C = |O:C$_{SOA}$-O:C$_{HOA}$|. A clear trend can be observed between the number of phases and the ΔO:C, with one- and two-phase particles forming for low and high ΔO:C values, respectively. Using a threshold of ΔO:C = 0.265 (black-dashed line in Fig. 2), we are able to predict the number of phases of 92% of the HOA + SOA mixtures studied in our experiments [3].

Overall, our results suggest that the difference in average O:C ratio of the organic components determine the number of phases in internally mixed HOA + SOA particles.
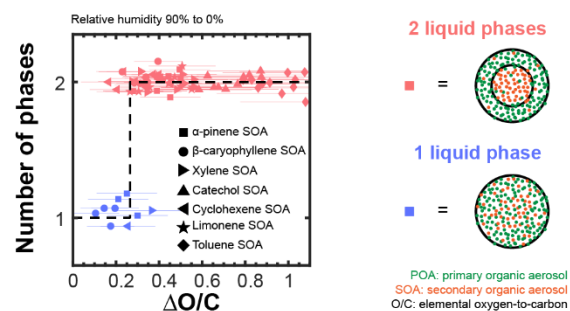
Fig. 2: Number of phases observed for HOA+SOA mixtures as a function of the difference in their O:C ratios (ΔO:C).

[1] J. L. Jimenez et al., Science, **326**, 1525-1529 (2009).

[2] F. Mahrt et al., Environ. Sci. Technol., **55**, 12202-12214 (2021).

[3] F. Mahrt et al., Environ. Sci. Technol., **56**, 3960-3973 (2022).

ATMOSPHERICALLY RELEVANT NANOPARTICLES AT LOW RH

J. J. Lin, K. Tumashevich (ATMOS), P. A. Alpert, M. Ammann, T. Bartels-Rausch (PSI),
N. L. Prisle (ATMOS)

We use X-ray excited electron spectroscopy at ambient water vapor pressures and with deposited, submicron aerosol particles of atmospheric relevance to study the interaction with water vapor below the deliquescence point.

The interaction between aerosol particles and water in the atmosphere has implications for air quality, human health, the hydrological cycle, and Earth's radiative balance. In particular, the surfaces of aerosol particles and aqueous droplets play important roles in regulating various atmospheric processes such as partitioning of water soluble gases, aqueous phase reactions, mobilization of ions, and phases changes.

Little is known about the process by which water vapor is adsorbed onto particles below their deliquescence point [1] since traditional aerosol instrumentation relies on detecting changes in the particle's volume or mass. Previous measurements using XPS [2] have detected changes in the chemistry at the particle surface in the presence of low amounts of water vapor for several compounds of atmospheric relevance. Here, we use the capabilities of the In-situ Spectroscopy beamline at SLS to provide chemically specific information at the particle surface at significantly higher relative humidities than previously reported [3].

The particles studied here were composed of pure malonic acid—a hygroscopic dicarboxylic acid commonly found in ambient aerosol samples—and malonic acid mixed with sodium chloride (NaCl) in molar ratios of 1:2, 1:1, and 2:1. Samples were prepared by nebulizing dilute solutions of malonic acid and NaCl, drying the generated droplets, and depositing the particles onto gold foil using an electrostatic precipitator. XPS measurements targeting the C 1s, O 1s, Na 1s, Cl 2p, and Au 4f core orbitals as well as Na and O K-edge NEXAFS measurements were performed at ultra-high vacuum and 1.25, 5, 15, and 26% relative humidity (RH). A schematic is shown in Fig. 1.
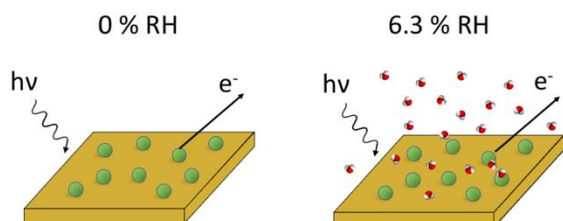
Fig. 1: Schematic of the experiment showing nanoparticles deposited onto gold foil at varying ambient relative humidity.

Fig. 2 shows the C 1s spectra for particles composed of 2:1 molar ratio malonic acid and NaCl for all five relative humidity values measured. The binding energy scale has been calibrated using the Au 4f spectra of the substrate. A shift in binding energy with increasing ambient water vapor can be seen, suggesting a change in the chemical environment starting at very low RH with the introduction of water vapor. Further analysis of the peak fits to the C 1s spectra can reveal potential keto-enol tautomerism occurring in the malonic acid [4]. Loss of chlorine can also be seen by changes in the peak intensity of chlorine compared to sodium with increasing RH.
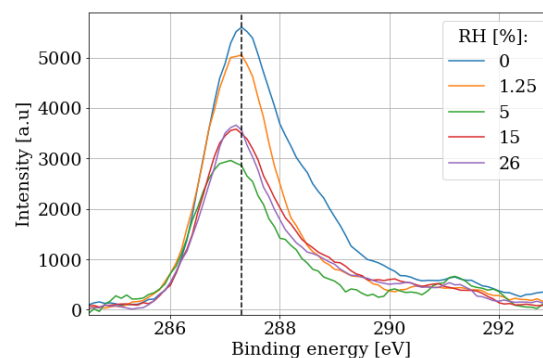
Fig. 2: XPS spectra for the C 1s orbital from malonic acid/NaCl particles (2:1 molar ratio) at 0, 1.25, 5, 15, and 26% RH.

These measurements suggest the possibility of chemical transformations that can influence atmospheric chemistry at RH values much lower than previously expected.

[1] M. E. Wise et al., Aerosol Sci. Tech., **42**, 281-294 (2008).
[2] J. J. Lin et al., Atmos. Chem. Phys., **21**, 4709-4727 (2021).
[3] F. Orlando et al., Top. Catal., **59**, 591-604 (2016).
[4] S. Yamabe et al., J. Phys. Chem. A, **108**, 2750-2757 (2004).

STXM CHARACTERISATION OF SALT FROM SYNFUEL PRODUCTION

P. A. Alpert (PSI), K. Kilchhofer (PSI & ETHZ), K. Y. Cheung (PSI LAC), A. S. H. Prévôt (PSI LAC),
L. Torrent, C. Ludwig (PSI LBK), T. Fovanna, G. Peng (TreaTech), F. Vogel, H. Xiang, D. Baudouin (PSI LBK),
M. Ammann (PSI)

Here, we use X-ray spectromicroscopy to characterize particles and soluble material from a continuous flow supercritical salt separator as a first step to convert bio-waste into sustainable upgraded fuel.

Hydrothermal gasification (HTG) and liquefaction (HTL) are techniques used to convert various biogenic feedstocks, such as microbial cultures, sewer sludge, black liquor and waste wood sawdust into sustainable gaseous and liquid fuels, respectively. They are currently being developed at the Bioenergy and Catalysis Laboratory at the Paul Scherrer Institute (PSI) in the Catalytic Process Engineering (CPE) group lead by F. Vogel. These processes operate in or near supercritical water and heavily rely on the selective removal of salts and/or unwanted carbonaceous particles [1]. The efficient recovery of brine (water and salts) is very important to protect any trap or catalyst that is used downstream, and relevant for recuperating costs by producing fertilizer [2]. On the other end, understanding the formation and the fate of carbonaceous particles during such process is of great importance to optimize biocrude or biogas production.

To investigate these challenging aspects, our main strategy is building novel capabilities for product stream analytics in multidisciplinary collaboration between the CPE group, the Chemical Processes and Materials (CPM) group headed by C. Ludwig, and the Surface Chemistry Research Group led by M. Ammann. Here, we report on the chemical characterization of particles and soluble compounds in sewer sludge feed and in the brine removed by the PSI salt separator [2] installed upstream a catalytic supercritical water HTG step to produce methane. Aliquots of the feed and the brine were centrifuged, and the supernatant and the re-suspended solids in water were analyzed using a transmission electron microscope (TEM) and scanning transmission X-ray microscopy coupled to near edge X-ray absorption fine structure (STXM/NEXAFS) spectroscopy. Morphology and carbon, oxygen and calcium bonding in single particles are presented.

Fig. 1A) shows spectra of feed and brine samples, where the measured optical density (i.e. X-ray absorption) is plotted as a function of X-ray energy. Functionalities corresponding to specific peaks are indicated. The main features are oxygenated organic ketones and carboxyl functionalities, and finally carbon double bonding. Solids (red and green) show a graphitic peak similar to soot around 293 eV. A TEM image of the brine solids shown in Fig. 1b reveals typical coke-like nanoparticles, which are carbonaceous particles likely formed from polymerized molecules with carboxylic functions [3, 4]. There is not much difference between spectra of the solids (red and green) and supernatants (blue and black). This further indicates the carbon removed from the feed is polymerized into coke having similar functionality. This information will help improving continuous salt and particle extraction and future catalyst selection toward these highly oxygenated compounds.
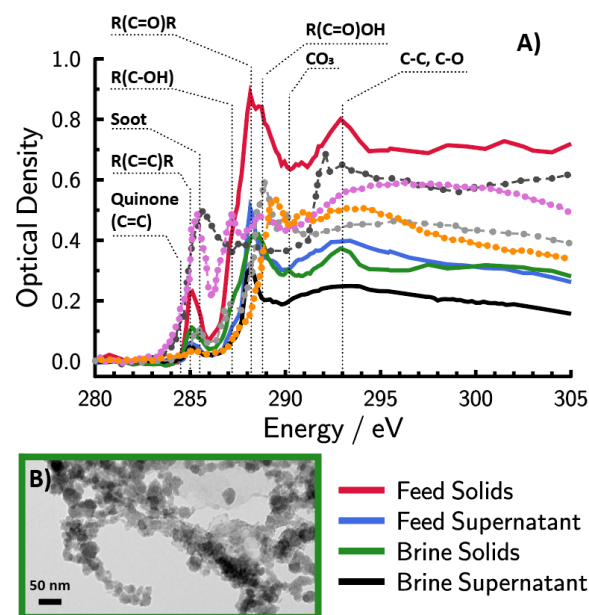
Fig. 1: A) Representative NEXAFS spectra of material in the feed into the salt separator and brine removed. The solids and supernatant after centrifugation is indicated in the legend. All spectra are background subtracted. Reference spectra of soot (dark grey) [5], tar balls (light grey) [5], lignin (purple) [6] and cellulose (orange) [6] are shown for comparison. B) TEM image of solid particles in the brine.

---

[1] M. Schubert et al., The Journal of Supercritical Fluids, **61**, 44-54 (2012).
[2] J. Reimer et al., The Journal of Supercritical Fluids, **117**, 113-121 (2016).
[3] M. Guisnet et al., Applied Catalysis A: General, **212**, 83-96 (2001).
[4] J. B. Müller et al., The Journal of Supercritical Fluids, **70**, 126-136 (2012).
[5] A. V. Tivanski et al., J. Phys. Chem. A, **111**, 5448-5458 (2007).
[6] C. Karunakaran et al., PLOS ONE, **10**, e0122959 (2015).

ADSORPTION – DESORPTION KINETICS AND THERMODYNAMICS

D. Knopf (SBU), M. Ammann (PSI)

Adsorption and desorption are crucial steps in all phase change processes at environmental interfaces. We have presented a consistent statistical thermodynamic treatment of equilibria and kinetics providing surprising insights into established features.

Desorption of a molecule from a surface is an essential elementary process that, together with reaction on the surface, entering the bulk phase, and reaction and diffusion therein, determines the life-time of this molecule on the surface. Desorption is an activated process involving a transition state (TS). In complete analogy to classical transition state theory (CTST) for gas phase reactions, the description of desorption kinetics requires formulation of the equilibrium between the TS and the adsorbed state. However, adsorption thermodynamics is rarely comprehensively treated in textbooks. We have thus retraced these developments with consistent terminology [1], based on other recent and earlier attempts in this direction [2,3].

The two simplest models of adsorption are the 2D ideal gas (*2D*) model, in which the molecules have two translational degrees of freedom parallel to the surface, and the 2D ideal lattice gas (*latt*) model, in which the molecules are bound to a limited number of equivalent surface sites. The latter is consistent with the well-known Langmuir adsorption model. Formulation of adsorption thermodynamics is based on the definition of activities. While straightforward for the *2D* case, where the surface coverage, θ, evolves linearly with the gas phase activity (proportional to pressure or number density), a proper and meaningful definition of the activity for the *latt* case is [1,2]

$$a_{latt} = \frac{\theta/(1-\theta)}{\theta_0/(1-\theta_0)} \ , \tag{1}$$

where θ_0 is a suitably chosen standard state [2]. This activity definition leads to the well-established dependency of θ on the gas phase number density, exhibiting saturating surface coverage at high number density in the form of the Langmuir isotherm. Applying the proper partition functions and linking these to the thermodynamic quantities allows to express the adsorption equilibrium constants in terms of both molecular and thermodynamic properties [1,2].

In turn, we have used this adsorption thermodynamics to formulate TS theory for desorption and to derive desorption rates and pre-exponential factors (*A*). For instance, this allows calculating the commonly used value of *A* for the *2D* case of 10^{13} s^{-1} from basic principles, but also the deviation from this value for the *latt* case. One of the most striking results is the non-first order behavior of the desorption rate for the *latt* case at high

θ (Fig. 1). The strong non-linearity is related to the diverging configurational entropy at high θ, driving the increase of the desorption rate. Experiments are often performed at high θ because of sensitivity limitations. However, they have commonly been analyzed assuming first order desorption behavior. Thus, they have led to erroneous desorption energies that cannot be extrapolated to low θ [1].

We have also applied the same approach to formulate adsorption rates, which have allowed us to derive the surface accommodation coefficient and to establish a link between adsorption thermodynamics and desorption kinetics [1,4].
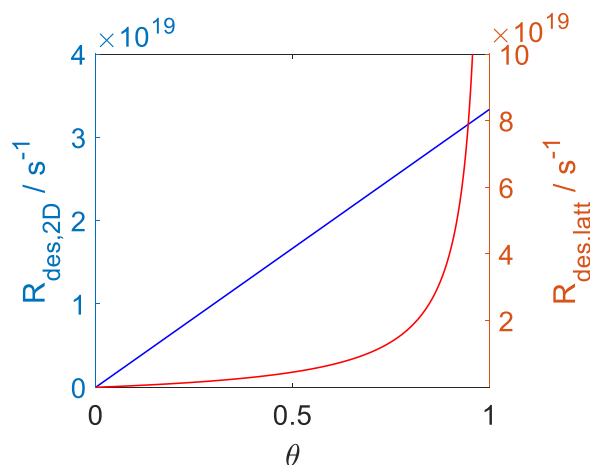
Fig. 1: The desorption rate for the case of a 2D ideal gas (blue line) and 2D ideal lattice gas (red line). Applied E_{des}^0 are 63 kJ mol^{-1} and 88 kJ mol^{-1}, respectively. We assume a desorption process without additional barrier, $E_b^0 = 0$.

[1] D. Knopf and M. Ammann, Atmos. Chem. Phys., **21**, 15725-15753 (2021).
[2] C. T. Campbell et al., J. Phys. Chem. C, **120**, 10283-10297 (2016).
[3] T. L. Hill, An Introduction to Statistical Thermodynamics, Dover Publications Inc. (1986).
[4] D. J. Donaldson et al., J. Phys. Chem. A, **116**, 6312-6316 (2012).

TRACE GAS DETECTION MEETS ELECTRON SPECTROSCOPY

T. Bartels-Rausch, A. Laso (PSI), C. Richter (FHI), L. Artiglia (PSI LSK & LUC), M. Ammann (PSI)

The ability to study both the gas-phase and surface coverage simultaneously is a key advantage for interfacial studies of atmospheric relevance. Here we describe modifications to the ISS endstation to dose and detect traces of gases.
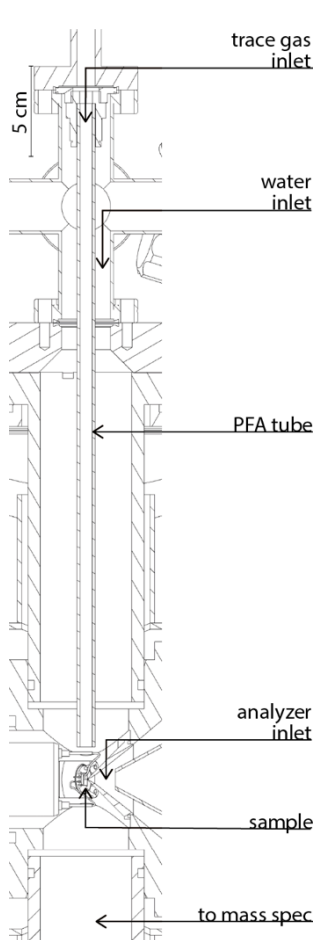
Fig. 1: Sketch of the ISS endstation showing the inert fluoropolymer (PFA) tube for trace gas dosing and the location of the mass spectrometer inlet.

Adsorption of trace gases to environmental surfaces and heterogenous reactions are a field of active research because these fundamental processes can impact atmospheric composition on a global scale [1]. Both, the adsorption, and the heterogeneous chemistry vary with the gas-phase partial pressure of the adsorbate/reactant [2].

The concentration of gases in experiments with relevance to atmospheric science spans orders of magnitude, from about 5 mbar water vapor to 1E-2 mbar of volatile organics, and 1E-6 mbar for acidic trace gases (Fig. 2).

Interaction of the trace gases at such low concentration with the walls of the gas delivery system may lead to loss and to slow response times [3]. To optimize transport, an inert fluoropolymer (PFA) transport line was introduced to the ISS endstation (Fig. 1). Separating the trace gas and water vapor transport improves the response time further.

Fig. 3 shows the dosing of phenol at low partial pressure with time as determined by a Hiden Quadrupole mass spectrometer situated downstream of the sample (Fig. 1). The detection limit of the mass spectrometer was found 4E-6 mbar making it ideal to detect volatile organics in the gas phase. Interestingly, the surface concentration on an ice sample initially reflects the increase of gas-phase concentration, before it saturates at higher

dosing. This is consistent with adsorption isotherms. Detailed analysis of the complete data set is ongoing.
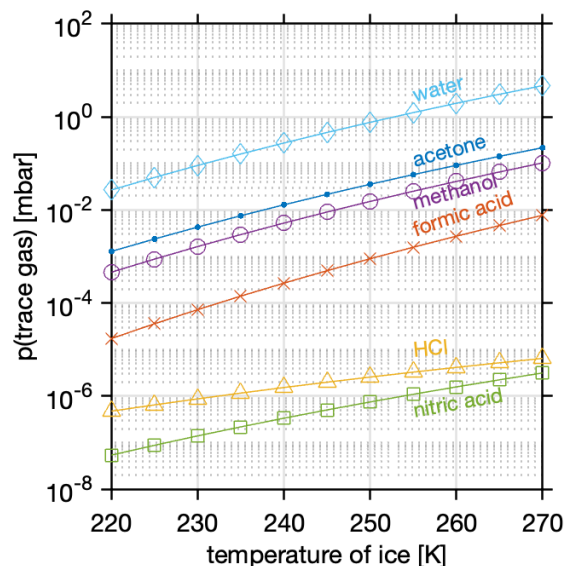
Fig. 2: Typical concentration of trace gases in experiments on the adsorption to ice surfaces [2].
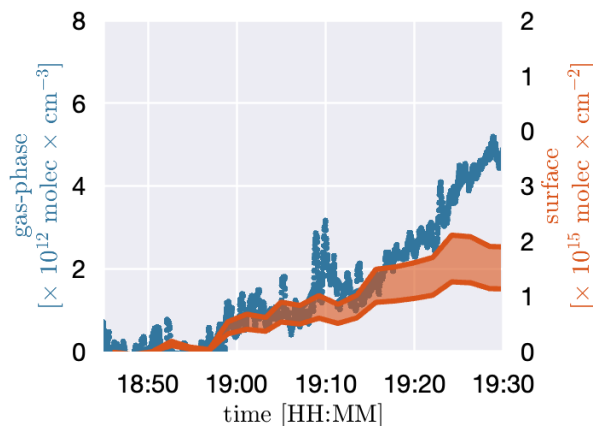
Fig. 3: Partial pressure of phenol as determined by mass spectrometry (blue line, left axis) and surface concentration of phenol adsorbed to ice based on calibrated X-ray photoemission spectra (red line, right axis). The shaded area represents uncertainties.

[1] A. M. Grannas et al., Atmos. Chem. Phys., **13**, 3271-3305 (2013).

[2] M. Ammann et al., Atmos. Chem. Phys., **13**, 8045-8228 (2013).

[3] J. A. Neuman et al., Environ. Sci. Technol., **33**, 1133-1136 (1999).

INTERACTION OF HEXYLAMINE WITH ICE

J. P. Gabathuler, Y. Manoharan (PSI & ETHZ), L. Artiglia (PSI LSK & LUC), T. Bartels-Rausch,
M. Ammann (PSI)

Amines are ubiquitous atmospheric bases and play an important role in neutralizing atmospheric acids. We report here first experiments of the adsorption of hexylamine on ice using near ambient pressure X-ray photoelectron spectroscopy (XPS).

As snow on the ground or cirrus clouds in the upper troposphere, ice plays a major role in the radiative budget of the Earth because of its high albedo. In addition, ice provides a large surface area for trace gas – ice interactions, which influence the chemistry of the atmosphere [1]. Amines are emitted from natural and anthropogenic sources [2]. Together with ammonia, they neutralize acids and substantially contribute to the formation and burden of particulate matter. Amines are semi-volatile, thus occurring in both the gas and particle phase. Looking into adsorption of an amine on ice allows studying the response of the ice surface to bases and contributes to the question of interfacial acidity. Here, we choose hexylamine (HA) as a first example.

XPS provides us with chemically selective surface composition information from the surface of ice equilibrated with its vapor pressure. After growing, stabilizing and characterizing the ice at -23°C with XPS as in previous work [3], we started dosing HA from the headspace of a liquid HA solution by means of a leak valve. During this procedure, we kept the X-ray photon energy constant at 1000 eV at the same spot on the ice surface, while iteratively monitoring the N1s and O1s core level photoemission spectra while step-wise opening the leak-valve. The absolute partial pressure of hexylamine is too low to be measured with a pressure gauge, but the spectra clearly reveal the increasing presence of nitrogen at the surface. Fig. 1 shows iteration #3 of the N1s spectra of hexylamine on ice at -23°C. The width of the peak indicates the presence of at least two components that we tentatively assign to $R–NH_2$ and $R–NH_3^+$.
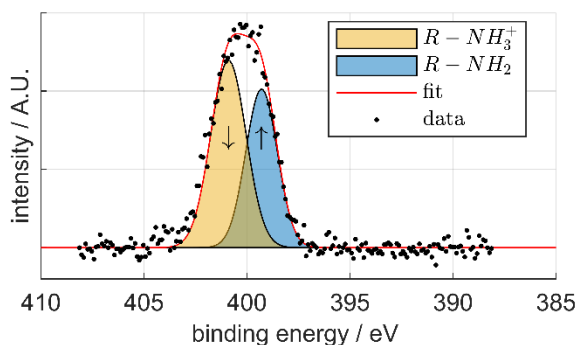
Fig. 1: N1s spectrum of hexylamine on ice, from iteration #3. Arrows indicate the evolution of the peaks with increasing hexylamine partial pressure.

Fig. 2 shows a proxy for the N/O elemental ratio, obtained as the ratio of the N 1s and O 1s peak areas, each normalized to the total cross-section of the two core levels at 1000 eV, but not considering the different inelastic mean free paths for the photoelectrons with different kinetic energy.
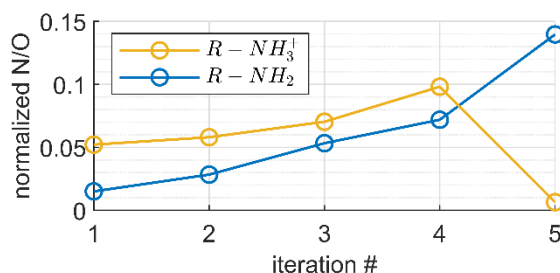
Fig. 2: Normalized N 1s to O 1s signal intensity ratio for $R–NH_2$ and $R–NH_3^+$. The hexylamine partial pressure is increased between each iteration.

The O 1s signal originates from the oxygen in H_2O, thus ice. Since the amount of ice probed is assumed to stay almost constant with increasing HA pressure, the N/O is expected to increase with increasing surface coverage of HA. From iteration #1 to #4, we observe an increase in both $R–NH_2$ and $R–NH_3^+$. The fact that already measurable signal was observed in the first iteration results from test experiments with HA on the sample holder performed prior to this experiment, so that HA desorbing from the chamber walls was leading to a signal already prior to opening the leak-valve. In an attempt to interpret the observed N/O ratios quantitatively, even the lowest observed N/O was higher than the ~0.01 expected for a monolayer of HA on ice so that we likely had a multilayer covering the ice. In iteration #5, we observe that the $R–NH_2$ increase while $R–NH_3^+$ vanishes. Our interpretation is that the supply of HA was high enough to condense and/or melt the surface by formation of a solution. From the endoscope image, bubbles were visible, suggesting the formation of bilayers or other complex structures.

Further experiments at much lower HA partial pressures are needed to explore the adsorption isotherm of HA on ice as well as to assess the degree of protonation.

[1] J. G. Dash et al., Reports on Progress in Physics, **58,** 115-167 (1995).
[2] X. Ge et al., Atmos. Environ., **45**, 524-546 (2011).
[3] A. Waldner et al., Phys. Chem. Chem. Phys., **20**, 24408-24417 (2018).

PHENOL ADSORPTION ON ICE MONITORED BY IN SITU XPS

C. Richter, R. Dupuy (FHI), L. Artiglia (PSI LSK & LUC), M. Ammann, T. Bartels-Rausch (PSI), H. Bluhm (FHI)

Air-water and air-ice interfaces are omnipresent in nature. Here we report on the adsorption of organic pollutants on the air-ice interface monitored by ambient pressure X-ray photoelectron spectroscopy.

Ambient pressure X-ray photoelectron spectroscopy (XPS) has been established as important technique to investigate liquid-vapor and ice-vapor interfaces [1]. This technique is particularly useful to study the electronic structure and chemical composition at the interface, which allows gaining direct insight into complex chemical reactions at aqueous interfaces, which are highly relevant in environmental and atmospheric science. This information is paramount to improving current models of atmospheric reactions.

Our investigation focusses on the interaction of phenol with ice, since phenol and other phenolic compounds are toxic organic pollutants produced by anthropogenic and natural sources and can be regularly found in the atmosphere and the aquatic environment, such as the snowpack.

We have used the ambient pressure XPS endstation in conjunction with the ISS beamline at SLS, which allows for the study of ice surfaces using the cryo-sample holder [2]. With this instrumentation we performed in-situ experiments on the uptake of gaseous phenol on the ice surface over the temperature range from 213 to 253 K.

Ice samples were grown by adjusting the water vapor pressure in the experimental cell to the equilibrium vapor pressure of water at the respective temperature of the sample holder. The uptake experiment was then performed by exposing the ice sample to a stream of phenol in a N_2 carrier gas. The adsorption of phenol was monitored by recording C1s and O1s spectra during continuous increase of the phenol partial pressure in the sample cell. Fig. 1 (a) and (b) show representative core level spectra recorded at hv = 900 eV and at a pressure of 0.99 mbar (water + phenol in N_2). In the C1s region the signal is comprised of phenol and an unknown carbon contamination. The phenol features in this deconvolution were constrained by data acquired previously in aqueous solutions of phenol [3]. The O1s signal shows a small gas phase peak due to water vapor and a condensed phase contribution due to ice.

From these spectra the C/O ratio corrected by the respective photoionization cross section and the electron signal attenuation by the gas phase was then used to reveal the uptake behavior of phenol. Fig. 1 (c) shows the C/O ratio as a function of the mass signal m/z = 94 (phenol). The mass signal was recorded by a quadrupole mass spectrometer attached close to the sample. It monitors the gas-phase composition, and the mass signal is proportional to the phenol partial pressure in the experimental cell. While the signal of the carbon contamination stays relatively constant, the signal intensity of phenol increases non-linearly with increasing phenol partial pressure. At first glance the C/O ratio resembles a Langmuir isotherm.

Further data analysis is ongoing for a more reliable characterization of the uptake process of phenol at the ice surface. The next round of experiments will focus on the heterogeneous reaction of phenol with reactive trace gases at the ice surface.
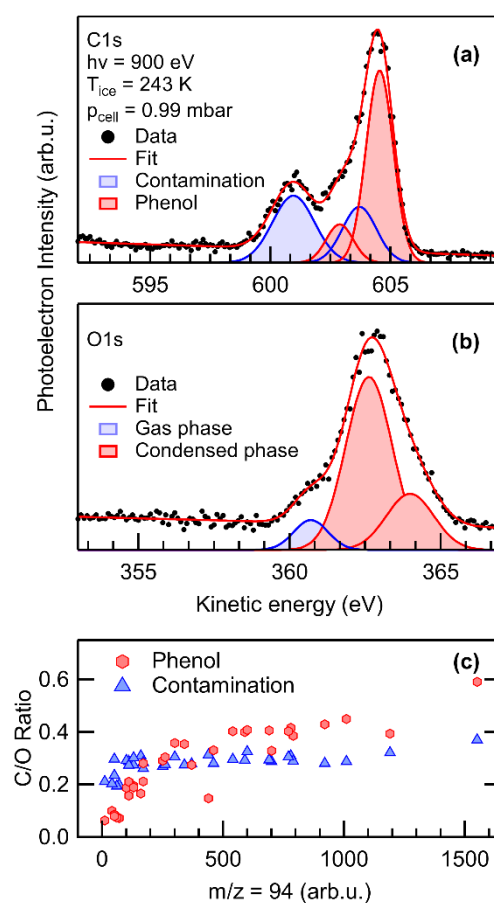
Fig. 1: (a) C1s and (b) O1s core-level spectra. (c) C/O ratio as a function of the m/z = 94 signal (proportional to the phenol partial pressure and total pressure in the experiment). The respective pressure range covered in this experiment corresponds to 0.35 – 1.0 mbar.

[1] R. Dupuy et al., J. Chem. Phys., **154,** art. no. 060901 (2021).
[2] F. Orlando et al., Top. Catal., **59**, 591-604 (2016).
[3] J. L. Solomon et al., Surf. Sci., **255**, 12-30 (1991).

GOODBYE BRØNSTED – HELLO INTERFACIAL ACID-BASE

T. Bartels-Rausch (PSI), C. Richter (FHI), Y. Manoharan (PSI & ETHZ), L. Artiglia (PSI LSK & LUC), M. Ammann (PSI)

The acid-base equilibrium is a central concept in chemistry. Experiments on the temperature trend of the dissociation at the ice surface support a unique mechanism of interfacial dissociation.
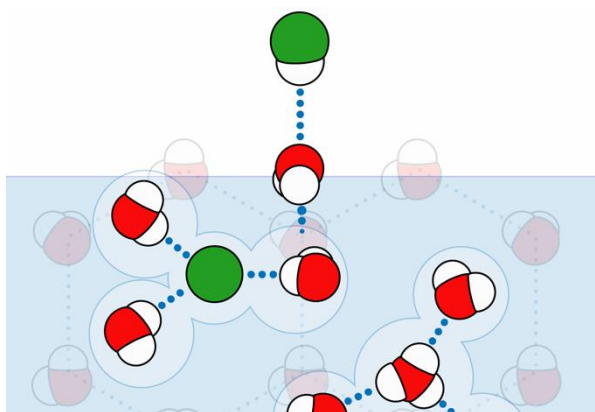
Fig. 1: Illustration of the dissociation of HCl (green spheres) in the interfacial region of ice (red spheres) upon adsorption [1].

The dissociation of acids at the air-ice interface is linked to their tendency to form hydrogen bonds with water molecules [2]. This requires flexibility in the hydrogen bonding network as water molecules need to rotate and twist away from the more rigid alignment in hexagonal ice (Fig. 1). Fig. 2 shows a larger dissociation degree of acetic acid at the ice surface with increasing temperature. This finding supports the impact of the interfacial disorder at ice surfaces, which increases with temperature [3], on chemistry. The photoelectron spectra of acids reveal the protonation degree, because electrons emitted from these molecular forms have different kinetic energies [4]. We found a dissociation degree of 30% at -55°C, and of 50% at -25°C. This trend is in excellent agreement with previous studies, giving 40% at -40°C. Further comparison with the temperature trend of dissociation in aqueous solutions is ongoing. Surface coverage in these experiments was approximately 10^{14} molecules per cm^2.

---

[1] X. Kong et al., J. Phys. Chem. Lett., **8**, 4757-4762 (2017).
[2] J. P. Devlin et al., Nature, **417**, 269-271 (2002).
[3] T. Bartels-Rausch et al., Atmos. Chem. Phys., **14**, 1587-1633 (2014).
[4] A. Krepelova et al., J. Phys. Chem. A, **117**, 401-409 (2013).
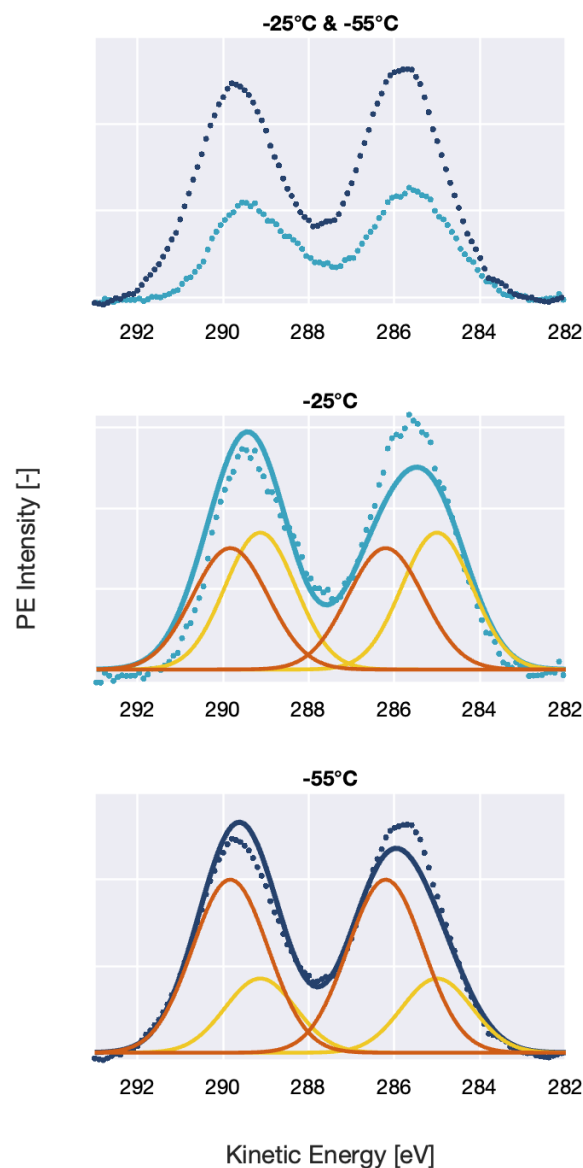
Fig. 2: Carbon 1s X-ray photoelectron spectra of acetic acid adsorbed to ice at -25°C (light blue dots) and at -55°C (dark blue dots). The two gauss-shaped features originate from the methyl- and from the carboxylic carbon of acetic acid. Also shown are deconvolutions of the signal revealing the dissociated (yellow) and undissociated fraction (red) of the acid at the air-ice interface. The slight underestimation of the methyl group's deconvoluted signal might indicate beam induced damage of the acetic acid, detailed analysis is ongoing.

The result suggests that dissociation at the interface is not an equilibrium process as it is in water, but depends on the molecular structure of the interfacial region.

CROSS-DATING A COLLE GNIFETTI SHALLOW ICE CORE

C. J. Huber (PSI & Univ. Bern), A. Eichler, S. Brütsch, F. Burgay, T. M. Jenk (PSI),
M. Schwikowski (PSI & Univ. Bern)

A 21 m shallow ice core from Colle Gnifetti recovered in 2021 was cross-dated with previously drilled ice cores. The major ion signals are nicely preserved, which is a prerequisite for future studies of organic tracers in this shallow core.

High-alpine ice cores allow access to pollution records back to pre-industrial times. However, these natural archives are in danger of melting. Recently Sommer et al. [1] stated that all zones of the glaciers in the Alps are experiencing melt, including the accumulation zone. Since 1976, several ice core studies have been conducted on Colle Gnifetti, Monte Rosa, which is the highest ice core site in the Alps at 4450 m a.s.l. In June 2021 we collected a 21 m shallow core to investigate the preservation of organic tracers [2]. The limited amount and thickness of ice lenses observed in the shallow core suggests that surface melt water formation is still limited. For the analyses of organic tracers, the core was cut as soon as the cores arrived in the laboratory, in order to reduce possible contamination from storage in plastic sleeves. The obtained core was dated applying annual layer counting using stable isotopes (δ^{18}O) and the seasonal variation of major ions (e.g., ammonium (NH_4^+)). In Fig. 1a) the good agreement between the two δ^{18}O records from the cores collected on Colle Gnifetti in 2015 (CG15) and 2021 (CG21) for the overlapping period (1995-2015) is shown. In addition, we observe preservation of the concentration and seasonal cycle of NH_4^+ (Fig. 1b)), indicating that summer surface melt has had a negligible effect on the records.

To underline the preservation of major ions we compared annual averages and 5-year averages of major ion concentrations of CG15/CG03 and CG21. The sulfate (SO_4^{2-}) record is shown as an example in Fig. 2. Both, annual and 5-years averages agree well and reflect the continuous downward trend of sulfate concentrations as a positive consequence of air pollution control measures (Fig. 2). This shallow ice core will be analyzed for organic tracers. The results will serve as baseline to assess the effect of melting on organic tracers in the shallow ice core drilled on Grand Combin in 2020 where we observed substantial melt influence on the major ion records [3].
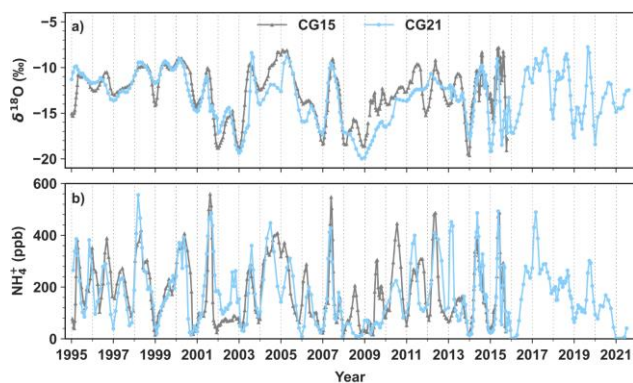
Fig. 1: Comparison of two records from ice cores drilled at Colle Gnifetti in 2015 and 2021. Good agreement for a) δ^{18}O and b) concentration of ammonium.

[1] C. Sommer et al., Nat. Commun., **11**, 3209 (2020).
[2] T. M. Jenk et al., p. 23 of this report.
[3] C. J. Huber et al., LUC Annual Report, p. 25 (2020).
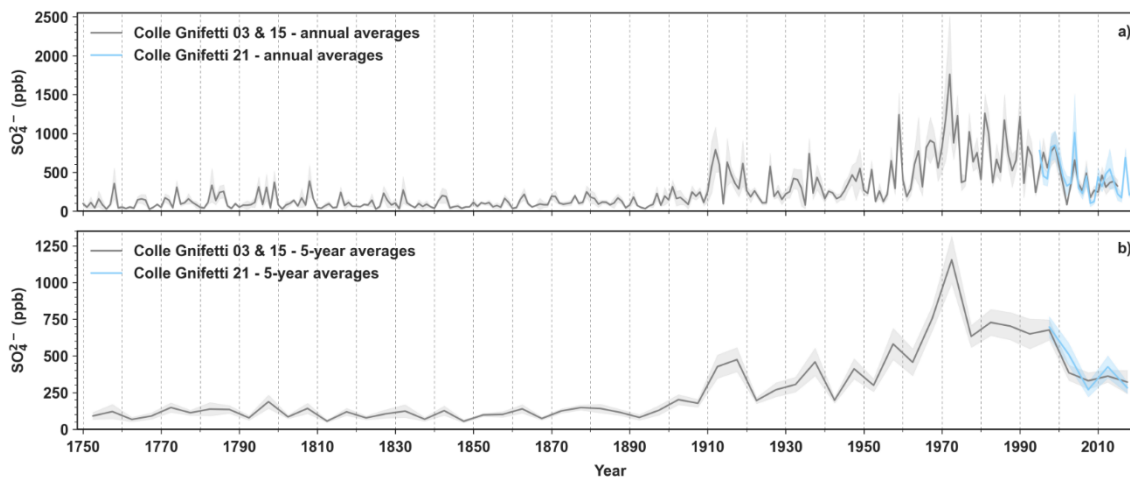
Fig. 2: Concentration records for sulfate from Colle Gnifetti shown as a) annual averages and b) 5-year averages covering the period of 1750-2015.

ICE MEMORY – DRILLING OF TWO DEEP ICE CORES FROM COLLE GNIFETTI

T. M. Jenk, F. Burgay (PSI), J. Gabrieli, F. de Blasi, A. Spolaor (CNR-ISP), P. Conz (Dolomiti Guides), R. Selvatico (Areaphoto), S. Harbeke (ZHdK), C. Barbante (CNR-ISP & Univ. Ca'Foscari), M. Schwikowski (PSI & Univ. Bern)

With the current warming, many valuable ice archives of past climate are in danger of being lost forever. Under the umbrella of ICE MEMORY, parallel ice (~80 m) and firn cores (~20 m) cores were drilled on Colle Gnifetti in June 2021. While one of the deep cores is aimed for preservation, as a heritage to posterity and future generations of scientists, the other cores will act as a reference.

The glacier saddle on Colle Gnifetti (Monte Rosa) is probably one of the best studied high elevation glacier sites in entire Europe. With 4450 m asl., it also marks the highest ice coring site in the Alps, first sampled in 1976. In this millennium, the Laboratory of Environmental Chemistry resampled the site with ice cores to bedrock in 2003 [1] and 2015 [2]. Within the framework of the international initiative ICE MEMORY (IM) [3], another site on Grand Combin was thus first aimed for in fall 2020. However, being at a lower elevation of 4100 m asl., it showed to already be too late to preserve a core from there [4, 5]. It also underlined that urgent action is needed. In 2021, PSI, in collaboration with the Ca' Foscari University of Venice, thus immediately invested in a new drilling expedition to Colle Gnifetti, recognized to likely be the last remaining site in the Alps to go for the objective of ICE MEMORY.

From 1-9 June, two parallel ice cores (82.7 m and 80.5 m), around 1.5 m distant from each other, were successfully extracted from the same spot sampled back in 2003 (45.92948° N, 7.87495° E; 4468 m asl.). In addition, two firn cores of 21 m (PSI) and ~15 m (Kovacs drill; Ca' Foscari) were collected, aiming, among other things, for investigation of the most recent effects and changes to the archive from warming [e.g. 6].
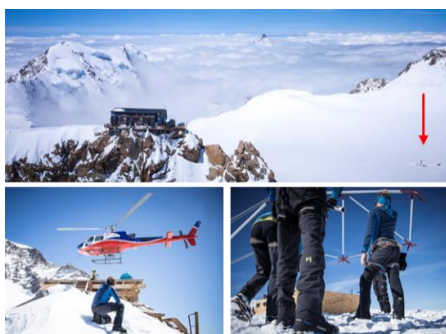
Fig. 1: Capanna Regina Margherita and drill site (red arrow). Bottom: Lift-off from Capanna Gnifetti and drill tent build-up.

For the operation, the Swiss and Italian teams started from their respective countries. The PSI team, starting by helicopter from Zermatt, unloaded and secured the drilling equipment on the glacier saddle and then continued to the Capanna Gnifetti (3650 m asl.) to team up with the Italian members for two nights of acclimatization (switch from Swiss to Italian helicopter required on Testa Grigia). All team members and the remaining equipment was then flown up from there on 3rd June, when the drilling tent and drill was set-up and the first 10 m were drilled. For the remaining period, the team was accommodated in the Capanna Regina Margherita (4554 m asl.). See Fig. 1.

Fig. 2: Drilling in progress and full commitment to use solar power even during snowfall

For drilling, the PSI electromechanical drill (icedrill.ch) was employed. For both cores, most of the drilling was performed using a stainless steel cutting ring. The first core, which was obtained with excellent ice core quality, surpassed a characteristic, thick dust layer just above bedrock (starting at ~80.6 m depth), so far only recovered in the 2003 core [7]. Slightly warmer temperatures and higher humidity in the second half of the operation aggravated drilling, which was then mostly conducted in the early morning or late evening/night. Despite the closeness of the two boreholes and drilling with similar settings, the ice core quality was partly worse for core 2, with sections recovered as brittle ice. Unfortunately, same depth as for core one could not be reached, likely because of hitting (a) small rock(s), preventing further ice perforation, see Fig. 2.

At the end of operation, all personnel and equipment including boxes with ice cores returned to their respective starting base by helicopter. The ice was then transported to the large freezer facilities for current storage (freezer truck or cooled by dry ice). See first results for the 21 m shallow analyzed at PSI in [6].

[1] T. M. Jenk et al., JGR, **114**(D14), D14305 (2009).
[2] M. Sigl et al., TC, **12,** 3311-3331 (2018).
[3] M. Schwikowski et al., LUC Annual Report, p. 23, (2020).
[4] T. M. Jenk et al., LUC Annual Report, p. 24 (2020).
[5] C. J. Huber et al., LUC Annual Report, p. 25 (2020).
[6] C. J. Huber et al., p. 22 of this report.
[7] D. Bolius, PhD Thesis, PSI/Uni Bern, 2006.

THERMAL DRILLING – A 224 M ICE CORE FROM ADAMELLO GLACIER

T. M. Jenk (PSI), M. Schwikowski (PSI & Univ. Bern), D. Stampfli (icedrill.ch), V. Maggi (Bicocca)

A 224 m long ice core was extracted from temperate ice in April 2021 on Pian di Neve (Adamello Glacier, Italy) using the PSI thermal drill.

The Adamello is the largest glacier in Italy with an extension of 16.3 km^2, but is located at a relative low elevation of 2500-3400 m asl.. At present, it is affected by considerable mass loss even in the (former) accumulation area. A shallow core drilled in 2016 showed, that despite the temperate glacier conditions with negative mass balance even on the high plateau (Pian di Neve, ~3100 m asl.), and consequentially an age of the ice surface different from the date of drilling (~20 years in 2016) this site has potential to still contain a valuable ice archive (1). Dating of the ice was shown to be possible and a variety of proxies in the ice can still be used for paleo interpretation. Based on a predicted thickness of around 270 m (ground penetrating radar), the Adamello ice archive was estimated to potentially cover significantly more than 1000 years of local and regional climate and pollution history [1].
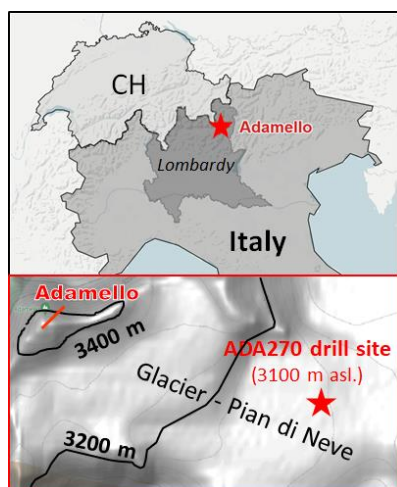
Fig. 1: Map showing the location of the summit of Adamello and the ADA270 ice core drill site on the Pian di Neve glacier.

The ADA270 field activities at the same location sampled in 2016 (617616, 5111580 WGS84 UTM32; see Fig. 1), took place in April 2021. The lead was by the University of Milano Bicocca (Italy), with funding from private and commercial donors as well as from regional and local municipalities, which also built up camp infrastructure (all transport by helicopter from/to Tému). The drilling itself was carried out by PSI (9.4.-16.4.) after a two-day travel by car and trailer (~1 t of equipment). The first 28 m were drilled electromechanically, until the borehole filled with water and required switching to the thermal drill module (2nd day). Thermal drilling was then conducted continuously (24 h/day) in three shifts (2-3 people each) to avoid closure of the

borehole due to the high dynamic of temperate ice flow. Fortunately, the water in the borehole never drained with a water table surface constantly around 30 m below surface, which helped to stabilize the borehole). Bedrock was finally reached on April 16 at a final depth of 224 m.
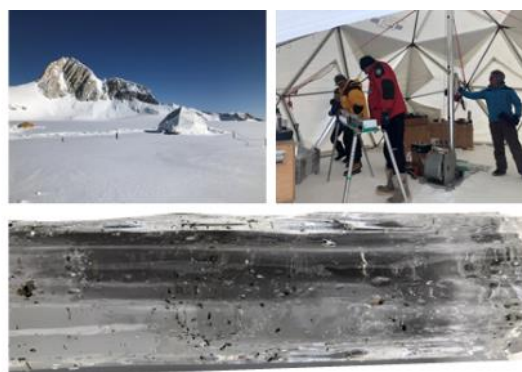
Fig. 2: Drill location and inside of the drill tent (top). Bottom most ADA270 ice core section. Note the crystal-clear ice (no dust from mechanical drilling) allowing to visibly recognizing ice crystal size and larger particles (dust/rocks, organic fragments).

New modifications on the thermal drill module proofed to be highly beneficial. Instead of using the motor of the electromechanical drill [2], a light, hollow frame was used as connection piece between cable (including power line) and drill. This allowed for much faster travel speed in the water-filled borehole due to reduced resistance from buoyancy when lowering the drill. Further, it helped shifting the center of mass much closer to the melt head, with mass now contained in a much heavier core tube. This made the drill behave more stable/steady while drilling. Together with the also improved melt-head (larger heated surface area), the drill speed was increased (2.5 m h^{-1} on average) and ice cores were more even in shape and bigger in diameter (~7.8 cm) compared to the previous version of the drill. A heat-cone ("Arnold"), as a replacement of the melt head allowed to (i) rim the borehole whenever it started to close off (every ~8 h at specific depths) and to (ii) subsequently remove dirt and even small rocks after being collected in the melted, confined small spot in the middle of the core cross section.

Currently, the ice is stored at EuroCold Lab in Milano awaiting analysis for a variety of parameters including dust, pollen and ^{14}C for dating.

[1]   D. Festi et al., TC, **15**, 4135–4143 (2021).
[2]   M. Schwikowski et al., AoG, **55**, 131-136 (2014).

TRACE ELEMENT ANALYSIS IN ICE COMPARING DIFFERENT INSTRUMENTS

T.S. Münster (PSI & Univ. Bern), T.M. Jenk (PSI), A. Eichler (PSI), G. Lee, C. Jensen (Univ. Bern),
M. Schwikowski (PSI & Univ. Bern)

By using optimized method procedures, the concentrations of trace elements (TE) in ice cores determined by different instrumental systems (ICP-TOF-MS and ICP-SF-MS) showed good agreement, both for soluble elements as well as for insoluble elements.

For analyzing TEs in ice cores, inductively coupled plasma mass spectrometry (ICP-MS) is the method of choice. Sector Field MS (ICP-SF-MS) has the advantage of high sensitivity and low detection limits. The benefit of Time of Flight MS (ICP-TOF-MS) is the faster analysis time even for a wide element spectrum; therefore, it can be used to measure single particles and their elemental composition.

Previous studies showed similar trends but differences in absolute concentrations of TEs in ice cores when using either instrument [1]. This effect was particularly evident for insoluble, and much less for soluble elements. For conventional TE analysis of ice cores at PSI, the samples are melted, manually acidified for 1 to 2.5 h and then measured with ICP-SF-MS. At the ICP-TOF-MS, incorporated into the continuous flow (CFA) system at the University of Bern, a continuous acidification is applied in the inlet system, less than 20 s before the measurement. Previous experiments showed that, depending on the time of acidification, large differences in concentration of TEs can be observed [2, 3]. Therefore we reduced the manual acidification prior to analysis by ICP-SF-MS to a still manageable short time of 1.5 min. An increase of the acidification time instead was not considered, because it could lead to dissolution of particles, prohibiting analysis of their elemental composition. Because of the inhomogeneity in environmental ice the use of aliquots would be preferential for most direct comparability between the two analytical systems. This was not possible because the instruments are located at different places. Previous experiments showed that element concentrations between aliquots of melted samples differed, unless acidified before [4]. This however will causes storage effects (even if refrozen), again most likely mainly related to a then increased time in acidification [2]. Therefore, separate, parallel samples were cut from the ice core of the Cerro Negro glacier (Chilean Andes, [5]) for this study.

With the above method optimizations in sample preparation, we achieved to significantly reduce the previously observed discrepancy of concentrations obtained with the two systems (Fig. 1). Similar to the previous results (2018 in Fig. 1, [1]), analysis applying new, optimized method procedures (2021) shows good agreement for soluble elements such as sodium (Fig. 1). However, for rather insoluble elements like lead, the optimization significantly improved the agreement between the results from the two systems (Fig. 1). This is

in agreement with our expectations, considering the fact that insoluble elements showed to be more affected by differences in acidification time [2, 3]. An explanation is that these elements are usually more strongly bound in minerals and thus harder to dissolve. While the small deviations at individual depths can be explained by the inhomogeneities in the ice, the average over all samples now shows near perfect agreement.
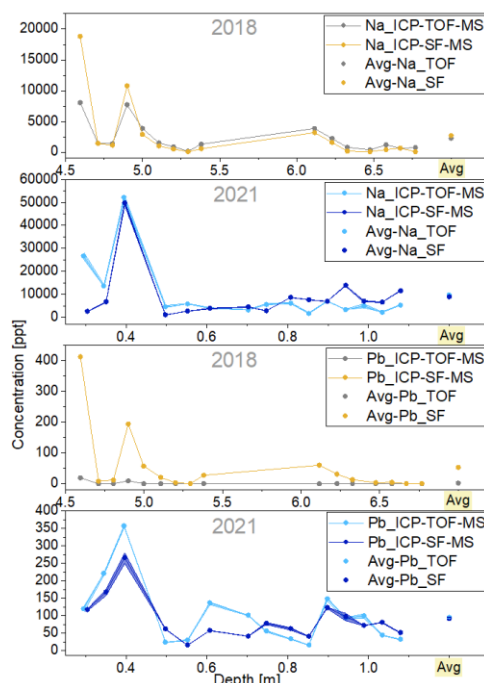
Fig. 1: Results from a previous study (2018, [1]) and new results with optimized method procedures (2021). Error bands show the standard deviation (n=3). The average over all samples is displayed to the right (Avg).

In a next step, we plan to use a desolvating nebulizer (Apex Omega) at the ICP-TOF-MS, similar to the ICP-SF-MS, allowing to achieve higher instrument sensitivity.

[1] J. Stegmaier et al., LUC Annual Report, p. 25 (2018).

[2] T. S. Münster et al., LUC Annual Report, p. 33 (2019).

[3] R. Rhodes et al., Chem. Geol., **286,** 207-221 (2011).

[4] T. S. Münster et al., LUC Annual Report, p. 29 (2020).

[5] M. Schwikowski et al., LUC Annual Report, p. 33 (2017).

EXTRACTING CARBONACEOUS AEROSOLS FROM GLACIER ICE

T. Singer (PSI & Univ. Bern), T. M. Jenk (PSI), M. Schwikowski (PSI & Univ. Bern)

The filter unit in the extraction system for dissolved organic carbon was modified, allowing now simultaneous extraction of all carbonaceous aerosol fractions from a single ice sample.

Atmospheric aerosols influence the climate in two main ways: directly by affecting the balance of incoming and outgoing solar radiation and indirectly by altering cloud properties. Carbonaceous aerosol is the dominant component of the total aerosol mass, accounting roughly 40% [1]. It consists of two major fractions, elemental carbon (EC) and organic carbon (OC). Based on its solubility, OC is further divided into dissolved organic carbon (DOC) and particulate organic carbon (POC). Natural archives, such as ice cores, provide access to samples representing past climate and atmospheric conditions, and thanks to radiocarbon (^{14}C) analysis, carbonaceous aerosols can be assigned to their original sources and used for dating [2].
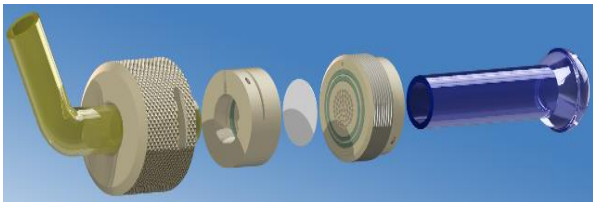
Fig. 1: The illustration shows an exploded view of the filter unit with all associated compression-fitting parts.

Two different setups have been used to extract carbonaceous aerosols from the ice. Until now, the insoluble carbonaceous particles were filtered onto preheated quartz-fibre filters using a dedicated glass filtration unit (hereafter referred to as POC-setup, [3]). Our goal was to implement a quantitative filtration step also in our DOC extraction setup [4].

Unrelated to the physical filtration of particles, the removal of carbonate from POC is also a crucial part of source apportionment. It was previously shown that ^{14}C dating based on DOC and POC yield similar ages [4]. Only samples with high dust content showed an age offset between the methods, which was attributed to incomplete removal of carbonates on the filter. So far, the the removal of carbonates from POC takes place in two steps: first, 20 ml of 1 M HCl is added to the melted ice before filtration, and second, the insoluble particles on the filter are acidified three times with 50 μl of 0.2 M HCl. The challenge is to ensure that both, filtration and carbonate removal efficiency, is high and reproducible (i.e. quantitative). The goal was to allow determination of all fractions (POC, DOC and EC) in a single ice sample. This would reduce requirement of valuable ice and time investment for sample preparation. We therefore performed (i) modifications to optimize the filtration setup of the DOC system and (ii) experimental tests to investigate its efficiency and (iii) improvements for carbonate removal from POC. For the latter, the question if acidification of the melted ice sample can be omitted prior to filtration was addressed (not possible if the filtrate is intended for subsequent molecular tracer analysis of the DOC fraction).

We implemented a new filter unit (Fig. 1) made out of polyetheretherketone (PEEK, characterized by excellent chemical resistance and easy to machine due to its mechanical properties) into the existing DOC setup. To ensure that the glass tube is pressed directly onto the filter, without shear forces leading to filter damage, a compression fitting was used. Two O-rings thereby support the filter and assure the assembly to be airtight. To test the efficiency and reproducibility of the filtration, a suspension of an Urban Dust (UD) reference standard (SRM 1649a) was used (I, Tab. 1). For testing the carbonate removal step (II, Tab. 1), we used a suspension of high concentration of Saharan dust with internal standard addition of UD.

The experimental results are shown in Tab. 1. The filtration with both setups yields (I) comparable amounts of carbon and F^{14}C values (in good agreement with the literature value [2]). The significant difference in mass and an isotopic mass balance calculation underlined the significant improvement of (II) carbonate removal by the new acidification procedure.

Tab. 1: Comparison of filtration efficiency (I) between the previous POC filtration and the filtration unit implemented in the DOC setup. Acidification test (II) with two different acid concentrations and their corresponding estimated removal efficiency.

(I) Filtration efficiency test		
Filtration method	mass C [μg]	F^{14}C*
DOC setup (n=6)	24.7 ± 3.3	0.72 ± 0.02
POC setup (n=6)	25.4 ± 3.8	0.71 ± 0.02
(II) Acidification test		
Acid concentration	mass C [μg]	removal eff.**
0.2 M HCl (n=2)	862.9 ± 43.3	91 ± 2 %
1 M HCl (n=3)	419.1 ± 21.2	~100 %

Literature values: *F^{14}C of UD: 0.70 ± 0.05 (OC) [2]; removal eff.: **95 ± 2 % [5]

[1]   K. E. Yttri, European Monitoring and Evaluation Programme EMEP (2007).

[2]   S. Szidat, Nuclear Instr. and Methods in Physics Research Section B, **223-224**, 829-836 (2004).

[3]   C. Uglietti et al., The Cryosphere, **10**, 3091-3105, (2016).

[4]   L. Fang et al., Radiocarbon, **61**, 681–694 (2019).

DATING OF AN ICE CORE FROM THE BELUKHA GLACIER

P. Nalivaika, T. Singer (PSI & Univ. Bern), V. Wilson (PSI & ÅAU), F. Burgay, S. Brütsch, T. M. Jenk (PSI),
T. Papina (IWEP), M. Schwikowski (PSI & Univ. Bern), A. Eichler (PSI)

The upper part of a new ice core recovered from the Belukha glacier in 2018 covers the period 1935-2018 and demonstrates a good agreement in the major ion records with the previously studied 2001 Belukha ice core.

A new 160 m ice core was drilled in June 2018 (B18) on Belukha glacier in the Siberian Altai (4060 m a.s.l., 49°48'27.7"N, 86°34'46.5"E) [1]. The drilling took place approximately 90 m NE of the drilling site, where a previous ice core was recovered in 2001 (B01). The obtained B18 ice core is used, among others, to reconstruct the recent heavy metal emissions from the former Soviet Union.

The upper 44 m (31.6 m w.eq.) of the B18 core were analyzed for major ions, water stable isotopes, black carbon and trace elements. This part was dated using a combination of independent methods: annual layer counting (ALC), tritium (^{3}H) dating, and cross-dating through a comparison of melt features, water stable isotope, and major ion records with the previously dated B01 core. The first dating attempt of the upper 26.5 m was performed a year ago, however, that record was lacking reference horizons [2]. Based on the new analyses we were able to confirm some of the old reference horizons and establish new ones. Accordingly, the five reference horizons of known age in the B18 core are (Fig. 1): (1) year 2018.5 at 0 m w.eq. (drilling date); (2) year 2001 at 10.5 m w.eq. (onset B01 core in the B18 records based on the agreement of Ca^{2+}, NH_4^+ and $exSO_4^{2-}$ records, and (3) similarity in strong melt features (20 cm and 24 cm thick ice lenses at 11.5 and 12.0 m w.eq. in the B18 core, respectively); (4) year 1963 at 23 m w.eq. based on the maximum in tritium [3]; (5) year 1935 at 31.6 m w.eq. based on the agreement in δ^{18}O records (end of the record). ALC based on the seasonal variation of δ^{18}O, NH_4^+ and $exSO_4^{2-}$ and black carbon (BC) was performed using the "IceCoreDating" software. Additionally, major ion records before 2001 of the two ice cores were synchronized, where possible, using a specialized "CoreMatch" software.

The new reference horizons have enabled us to establish a precise age-depth scale of the upper 31.6 m w.eq., covering the period 1935–2018. The dating resulted in a high accumulation rate of 0.60 m w.eq. for the B18 core between 2001 and 2018, and a much lower accumulation of 0.33 m w.eq. between 1935 and 2001 (Fig. 1). Currently we cannot explain the observed strong decrease in the accumulation rate. The accumulation rate of the B01 core for the corresponding period 1935-2001 was 0.48 m w.eq. The established time scale is corroborated by the good agreement between the major ion records of the two ice cores. NH_4^+ and $exSO_4^{2-}$ records of the B18 and B01 cores correlate well based on the

10-year mean concentration records (Fig. 2). General trends agree also for the annual records, whereas partial differences might be explained by the dating uncertainty, local variations in precipitation, wind-redistribution or glaciological effects.
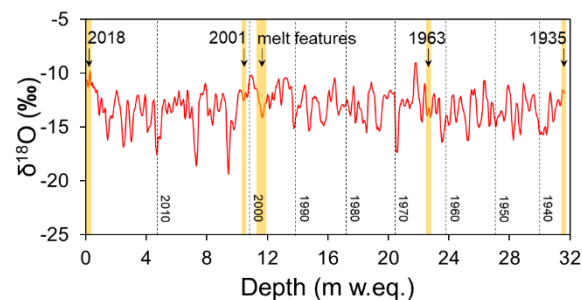
Fig. 1: δ^{18}O record (3-point moving averages) for the 2018 Belukha ice core (B18) together with reference horizons discussed in the text.
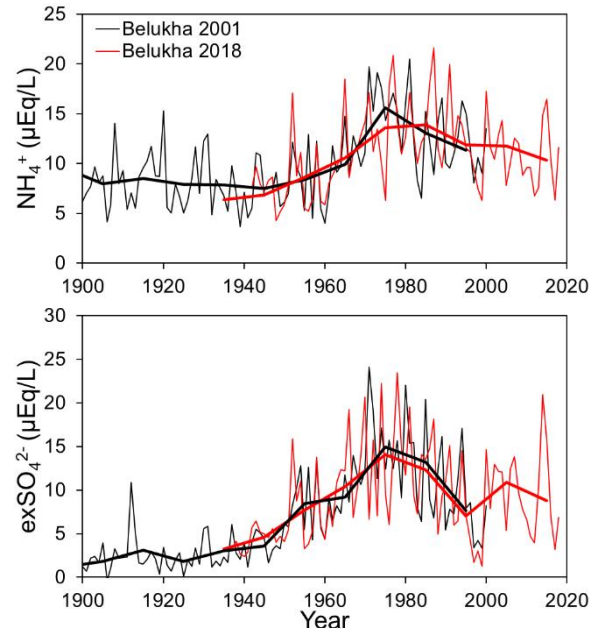
Fig. 2: NH_4^+ (top) and $exSO_4^{2-}$ (bottom) records for the B18 (red) and B01 (black) Belukha ice cores. Shown are annual (thin lines) and 10-year (thick lines) mean concentrations.

[1]   T. M. Jenk et al., LUC Annual Report, p. 31 (2018).
[2]   V. Wilson et al., LUC Annual Report, p. 31 (2020).
[3]   I. D. Clark and P. Fritz, CRC press (2013).

REFREEZING MOLTEN ICE SAMPLES AFFECTS THE QUALITY OF THE RESULTS

F. Burgay (PSI), D. Salionov, S. Bjelic (PSI LBK), A. Eichler (PSI), T. Singer, C. J. Huber,
M. Schwikowski (PSI & Univ. Bern)

The refreezing of previously molten ice samples has been frequently used as a strategy to temporary store samples. In this study, we demonstrate that this approach can affect the accuracy of the results.

To reliably identify and quantify organic compounds in ice and snow samples, it is fundamental to evaluate their stability and preservation along the entire analytical procedure. In some studies [1], molten ice samples were refrozen prior to analysis, but little is known about the preservation of the compounds in the samples during this step. Previous investigations performed on different chemicals (drugs) and matrices (wastewater) showed divergent results [2,3], indicating that case-specific studies are needed to assess the analytes' preservation when the samples are refrozen. In this context, we investigated the preservation of six organic tracers (syringic acid, vanillic acid, syringaldehyde, p-hydroxybenzoic acid and pinic acid) in refrozen ice samples.

To study this phenomenon on real ice and snow samples, we developed a new Solid Phase Extraction (SPE) methodology followed by a Ultra High Performance Liquid Chromatography and High Resolution Mass Spectrometry (UHPLC-HRMS) analysis. The method showed average recoveries of 76% (58-88%), excellent *inter*-day reproducibility, no significant matrix effects and fast analysis time (15 min per sample). The method detection limits for the different tracers, quantified as 3 times the standard deviation of the average value of the procedural blanks (n=16), were significantly lower than the concentration ranges observed in ice samples from different locations [4,5]. The instrumental accuracy and precision at 10 ng g^{-1} were between -0.01% and 0.4% and between 0.2% and 1.0% RSD, respectively.

The refreezing effect was investigated using different snow matrices and different analyte concentrations. The experiments are summarized as follows:

a) 400 g of snow were molten and spiked with the targeted compounds to reach a final spiked concentration of 0.1 ng g^{-1}. The sample was divided into 12 aliquots: 4 were extracted and analyzed the same day, the other 8 were frozen for 24 and 48 hours, respectively, then extracted and analyzed ;
b) as for a), but the spiked concentration was 0.03 ng g^{-1} ;
c) 2x30 mL real sample aliquots were spiked to reach a final added concentration of 0.03 ng g^{-1}. One aliquot was immediately extracted and analyzed, while the other was kept frozen for 7 days, then extracted and analyzed. This procedure was repeated for 6 different samples.

The results of the experiments (Fig. 1) show that the refreezing of previously molten ice samples led to a significant absolute mass loss that can affect the quality of the analysis, especially for those samples where the organic tracer concentrations were low (0.03 ng g^{-1}). We hypothesize that the reason of this phenomenon is the adsorption to the walls of the glassware used in this study [6].

In light of this, alternative sample storage strategies should be preferred. The freezing of loaded and dried SPE cartridges seems to be an effective approach in reducing mass losses [6], as also confirmed by specific investigations performed on the six targeted compounds used for this study on real ice samples *(not shown in this report)*.
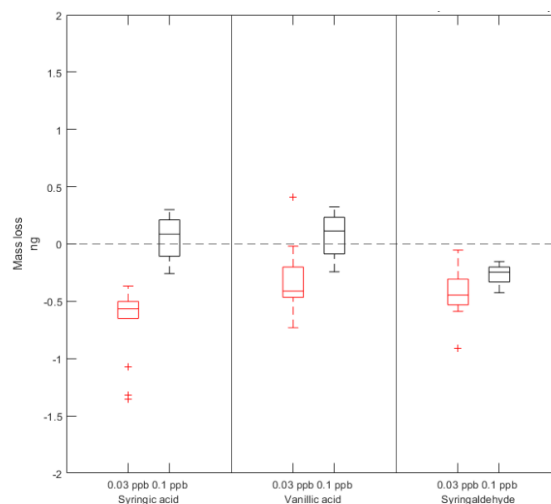
Fig. 1: Mass losses observed for syringic acid, vanillic acid and syringaldehyde in the 0.03 ng g^{-1} (n= 18, red bar) and in the 0.1 ng g^{-1} spiked samples (n = 12, black bar). The mass loss was more evident at the lowest concentrations for syringic and vanillic acid, while it was similar at both concentration levels for syringaldehyde.

[1] A. Vogel et al., Environ. Sci. Technol., **53**, 12565-12575 (2019).
[2] C. Chiaia et al., Environ. Sci. Technol., **42**, 8841-8848 (2008).
[3] D. R. Baker et al., J. Chromatogr. A, **1218**, 1620-1631 (2011).
[4] C. Müller-Tautges et al., Atmos. Chem. Phys., **16,** 1029-1043 (2016).
[5] M. M. Grieman et al., Clim. Past, **14**, 637-641 (2018).
[6] J. Carlson et al., Environ. Tox.. Chem., **32**, 337-344 (2013).

HEAVY METAL EMISSION ESTIMATES FOR THE FORMER SOVIET UNION (FSU)

S. Kakareka, T. Kukharchyk (INM Minsk), A. Eichler (PSI)

Cd, Cu, Hg, Pb, and Zn emission estimates for the territory of the FSU in the period 1975-2015 suggest a significant drop in emissions after 1990 following the economic crisis and disintegration of the USSR.

Air pollution from metallurgical industries and fossil fuel combustion in the FSU caused widespread damage on the environment and human health. The development of heavy metal emissions in this region during the last ~40 years is, however, not well understood and published data vary about one order of magnitude depending on the data source, as official statistical data or expert evaluations [1]. Here we provide new emissions estimates for the heavy metals Cd, Cu, Hg, Pb, and Zn. These data are used for cross-comparison and validation of ice-core heavy metal records obtained from glaciers in the Siberian and Mongolian Altai, influenced by emissions from the territory of the FSU [2].

The calculation of heavy metal emissions was performed based on (1):

$$(1) \quad E_{i,m} = V_m * F_{i,m} * V_{i,m}$$

($E_{i,m}$…emissions of metal i from sector m, tons;
V_m…production in sector m, million tons;
F_i…emission factor of metal i, g / t;
$V_{i,m}$…vector of emission factor of metal i in sector m).
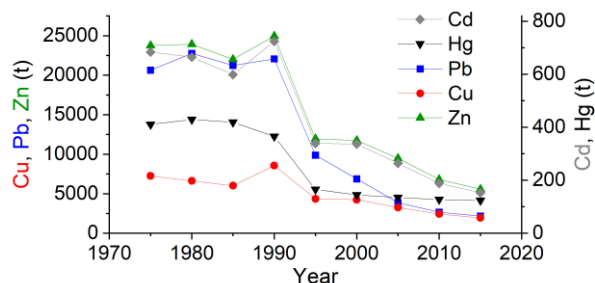
Fig. 1: Compilation of estimated Cd, Cu, Hg, Pb, and Zn emissions on the territory of the FSU.

Various sources have been used to infer production and emission quantities and factors (see e.g. [3-4]). Major emission sources during the investigated 40 years were copper production (Cu, Cd), or copper and steel production (Zn). Pb was mainly emitted from mobile sources until the phasing out of leaded gasoline in the late 1990s-2000s, later the main source was copper production (see Tab. 1). The main Hg emitter during the 40 years was fuel combustion (energy sector), caustic soda and mercury production before 1990.

Results of the estimates show high concentrations of all five investigated metals until 1990, a strong drop between 1990 and 1995, and decreasing values afterwards (Fig. 1). The strong drop after 1990 is related to the economic crisis of the USSR and its disintegration in 1991. The decreasing values afterwards are mainly due to the technological changes and implementation of abatement measures and the decrease in metal production.

Our new emission estimates allowed to significantly amend emission data officially submitted to the Convention on Long-Range Transboundary Air Pollution (LRTAP) to the EMEP programme, as well as expert estimates, prepared by the Centre on Emission Inventories and Projections (CEIP) [5] and Meteorological Synthesizing Centre - East (MSC-E) [6]. Slight differences to expert emission estimates of Cd, Hg, and Pb (years 1990, 1995) [1] are related to the improved method by the introduction of dynamic emission factors.

[1] S. Kakareka et al., Atmos. Env., **38**, 7101-7109 (2014).

[2] P. Nalivaika et al., this report p. 27.

[3] USGS website: https://www.usgs.gov/centers/nmic/commodity-statistics-and-information.

[4] S. Kakareka, Transboundary air pollution and its regulation. Minsk, Belaruskaya navuka (2009).

[5] EMEP CEIP website: https://www.ceip.at/webdab-emission-database/reported-emissiondata.

[6] EMEP MSC-E website: https://en.msceast.org/

Tab. 1: FSU Pb emission estimates (t) from different source sectors in the period 1975-2015.

Sector	1975	1980	1985	1990	1995	2000	2005	2010	2015
Fuel combustion (energy sector)	166.9	187.4	187.3	187.2	101.1	83	73.2	66.2	67.1
Fuel combustion (housing and communal sector)	20.4	21.1	21.3	22.2	3.5	1.2	3.2	4.9	2.7
Fuel combustion (domestic sector)	27.8	29.2	29.5	31.4	21.3	18.1	5.3	5.8	8
Primary lead production	2902.3	3174.3	2591.3	2089.4	481.9	657.5	312	230.9	229.4
Primary zinc production	334.7	378.4	375	333.9	155.7	159.4	137.7	77.4	69.2
Primary copper production	4545	4053.6	3656.5	5575.2	2825.6	2763.5	2053.2	1500.6	1186.8
Cement production	731.5	750	687.8	694.3	233.5	152.8	175.3	124.9	125.4
Nickel production	91.2	87	79.2	78.4	43.8	45.1	44.8	31	19.1
Steel production	2261.2	2368	2066.7	2068.2	911.2	937.8	776.1	576.3	431.4
Mobile sources	9504.3	11672.3	11517.4	10924.8	5042.5	2027.7	227.2	42.1	3.8
Others	46.3	28.3	20.5	57.1	55.6	27.7	62.6	8.3	25.1
Total	**20631.6**	**22749.6**	**21232.5**	**22062.1**	**9875.7**	**6873.8**	**3870.6**	**2668.4**	**2168**

PRE-INDUSTRIAL TO INDUSTRIAL CHANGES OF AEROSOL CONSTITUENTS

M. Schwikowski (PSI & Univ. Bern) for the Analytical Chemistry Group

Ice cores from mountain glaciers and polar ice sheets contain long-term records of aerosol constituents, which are indispensable to constrain model simulations of global aerosol radiative forcing.

There has been a tremendous improvement in the understanding of atmospheric aerosols and their climate effect over the last decades. However, due to the large complexity of atmospheric aerosols a robust quantification of their climate effect is still lacking. In contrast to long-lived, well-mixed greenhouse gases, aerosol particles have a lifetime in the atmosphere of about one week and show therefore a heterogeneous spatial distribution with highest concentrations close to the sources. In this context, ice core records of aerosol constituents are very valuable, since they are available from many regions in the mid- and high-latitudes, and allow reconstructing aerosol concentration, composition, and trends back to the pre-industrial period.

This is illustrated with the compiled ice-core sulphate and black carbon records in Figs. 1 and 2, respectively. Sulphate concentrations increased by a factor of 8 from the end of the 19th century to the 1970s in Europe, by a factor of 4 from the 1940s to the 1970s in Russia, and by a factor of 3 from the end of the 19th century to the 1950s in the Arctic (Svalbard). In all these regions, concentrations have declined since. In contrast, there is no anthropogenic peak in Antarctica, which is too remote from the sources and only a recent increase in South-America.
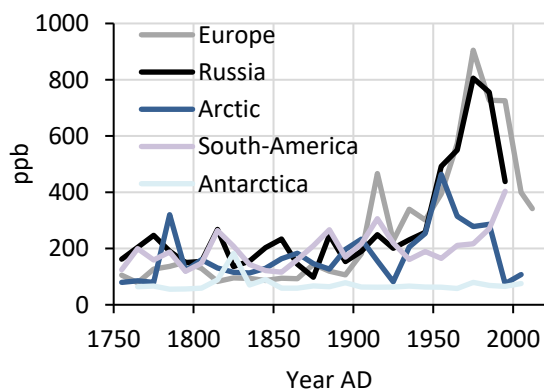
Fig. 1: Non-sea salt sulphate records from ice cores (10-year averages) from Europe (Colle Gnifetti [1]), Russia (Belukha [2]), the Arctic (Lomonosovfonna [3]), South-America (Illimani [4]), and Antarctica (stacked record including the four ice cores DIV2010, B40, Talos Dome, and DFS10 [5]).

The black carbon concentrations show trends similar to sulphate, except that the maximum in Europe and the Arctic (Svalbard and Greenland) was earlier, i.e. already in the 1920s. This is in contrast to black carbon simulations of 11 Earth system models of the latest generation, which show the main peak in the 1970s in Europe and Greenland, suggesting large uncertainties in the emission estimates used in these models [6].

Modified versions of the two figures are included in the newest IPCC report [7], whereby seven of the eleven data sets were produced by our group.
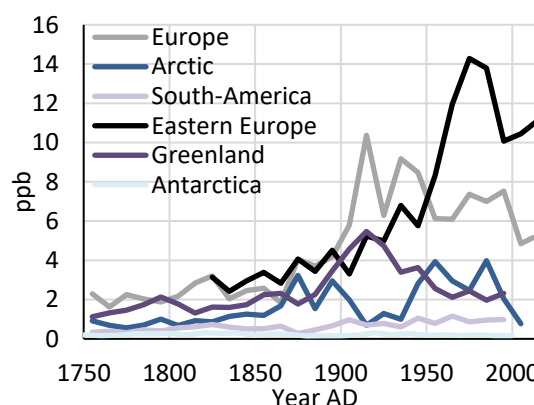
Fig. 2: Black carbon records from ice cores (10-year averages) from Europe (Colle Gnifetti [8]), the Arctic (Lomonosovfonna [9]), South-America (Illimani [10]), Eastern Europe (Elbrus [11]), Greenland (stacked record including the four ice cores NEEM-2011-S1, D4, TUNU2013, and Summit2010 [8 and references therein]) and Antarctica (B40 [12]).

[1] M. Enghardt et al., Tellus B, **69**, 1328945 (2017).
[2] A. Eichler et al., Geophys. Res. Lett. 36, L18813 (2009).
[3] I. A. Wendl et al., Atmos. Chem. Phys., **15**, 7287–7300 (2015).
[4] T. Kellerhals et al., JGR **115**, D16123 (2010).
[5] M. Sigl et al., Nature Climate Change, **4**, 693-697 (2014).
[6] K. O. Moseid et al., submitted to JGR.
[7] S. K. Gulev et al., 2021, In: Climate Change 2021: The Physical Science Basis. Contribution of Working Group I to the Sixth Assessment Report of the Intergovernmental Panel on Climate Change [V. Masson-Delmotte et al., (eds.)]. Cambridge University Press, in press.
[8] M. Sigl et al., The Cryosphere, **12**, 3311-3331 (2018).
[9] D. Osmont et al., Atmos. Chem. Phys., **18**, 12777–12795 (2018).
[10] D. Osmont et al., Clim. Past, **15**, 579–592 (2019).
[11] S. Lim et al., Atmos. Chem. Phys. 17, 3489-3505 (2017).
[12] M. Arienzo et al., JGR **122**, 6713-6728 (2017).

LIST OF PUBLICATIONS

SURFACE CHEMISTRY

P. A. Alpert, J. Dou, P. Corral Arroyo, F. Schneider, J. Xto, B. Luo, T. Peter, T. Huthwelker, C. N. Borca, K. D. Henzler, T. Schaefer, H. Herrmann, J. Raabe, B. Watts, U. K. Krieger, M. Ammann
Photolytic radical persistence due to anoxia in viscous aerosol particles
Nature Communications. 2021; **12**, 1769 (8 pp.). https://doi.org/10.1038/s41467-021-21913-x

R. Anthony Cox, M. Ammann, J. N. Crowley, P. T. Griffiths, H. Herrmann, E. H. Hoffmann, M. E. Jenkin, V. F. McNeill, A. Mellouki, C. J. Penkett, A. Tilgner, T. J. Wallington
Opinion: the germicidal effect of ambient air (open-air factor) revisited
Atmospheric Chemistry and Physics. 2021; **21**, 13011-13018. https://doi.org/10.5194/acp-21-13011-2021

T. Bartels-Rausch, X. Kong, F. Orlando, L. Artiglia, A. Waldner, T. Huthwelker, M. Ammann
Interfacial supercooling and the precipitation of hydrohalite in frozen NaCl solutions as seen by X-ray absorption spectroscopy
Cryosphere. 2021; **15**, 2001-2020. https://doi.org/10.5194/tc-15-2001-2021

S. Chen, L. Artiglia, F. Orlando, J. Edebeli, X. Kong, H. Yang, A. Boucly, P. Corral Arroyo, N. L. Prisle, M. Ammann
Impact of tetrabutylammonium on the oxidation of bromide by ozone
ACS Earth and Space Chemistry. 2021; **5**, 3008-3021. https://doi.org/10.1021/acsearthspacechem.1c00233

J. Dou, P. A. Alpert, P. Corral Arroyo, B. Luo, F. Schneider, J. Xto, T. Huthwelker, C. N. Borca, K. D. Henzler, J. Raabe, B. Watts, H. Herrmann, T. Peter, M. Ammann, U. K. Krieger
Photochemical degradation of iron(III) citrate/citric acid aerosol quantified with the combination of three complementary experimental techniques and a kinetic process model
Atmospheric Chemistry and Physics. 2021; **21**, 315-338. https://doi.org/10.5194/acp-21-315-2021

L. A. Garofalo, Y. He, S. H. Jathar, J. R. Pierce, C. D. Fredrickson, B. B. Palm, J. A. Thornton, F. Mahrt, G. V. Crescenzo, A. K. Bertram, D. C. Daer, J. L. Fry, J. Orlando, X. Zhang, D. K. Farmer
Heterogeneous nucleation drives particle size segregation in sequential ozone and nitrate radical oxidation of catechol
Environmental Science and Technology. 2021; **55**, 15637-15645. https://doi.org/10.1021/acs.est.1c02984

Y. Huang, F. Mahrt, S. Xu, M. Shiraiwa, A. Zuend, A. K. Bertram
Coexistence of three liquid phases in individual atmospheric aerosol particles
Proceedings of the National Academy of Sciences of the United States of America PNAS. 2021; **118**, e2102512118 (9 pp.). https://doi.org/10.1073/pnas.2102512118

A. Karagodin-Doyennel, E. Rozanov, T. Sukhodolov, T. Egorova, A. Saiz-Lopez, C. A. Cuevas, R. Fernandez, T. Sherwen, R. Volkamer, T. K. Koenig, T. Giroud, T. Peter
Iodine chemistry in the chemistry-climate model SOCOL-AERv2-I
Geoscientific Model Development. 2021; **14**, 6623-6645. https://doi.org/10.5194/gmd-14-6623-2021

K. Kilchhofer, F. Mahrt, Z. A. Kanji
The role of cloud processing for the ice nucleating ability of organic aerosol and coal fly ash particles
Journal of Geophysical Research D: Atmospheres. 2021; **126**, e2020JD033338 (21 pp.). https://doi.org/10.1029/2020JD033338

D. A. Knopf, K. R. Barry, T. A. Brubaker, L. G. Jahl, K. A. Jankowski, J. Li, Y. Lu, L. W. Monroe, K. A. Moore, F. A. Rivera-Adorno, K. A. Sauceda, Y. Shi, J. M. Tomlin, H. S. K. Vepuri, P. Wang, N. N. Lata, E J. T. Levin, J. M. Creamean, T. C. J. Hill, S. China, P. A. Alpert, R. C. Moffet, N. Hiranuma, R. C. Sullivan, A. M. Fridlind, M. West, N. Riemer, A. Laskin, P. J. DeMott, X. Liu
Aerosol–ice formation closure: a Southern Great Plains field campaign
Bulletin of the American Meteorological Society. 2021; **102**, E1952-E1971. https://doi.org/10.1175/BAMS-D-20-0151.1

D. A. Knopf, M. Ammann
Technical note: adsorption and desorption equilibria from statistical thermodynamics and rates from transition state theory
Atmospheric Chemistry and Physics. 2021; **21**, 15725-15753. https://doi.org/10.5194/acp-21-15725-2021

X. Kong, D. Castarède, E. S. Thomson , A. Boucly, L. Artiglia, M. Ammann, I. Gladich, J. B. C. Pettersson
A surface-promoted redox reaction occurs spontaneously on solvating inorganic aerosol surfaces
Science. 2021; **374**, 747-752. https://doi.org/10.1126/science.abc5311

B. Kärcher, F. Mahrt, C. Marcolli
Process-oriented analysis of aircraft soot-cirrus interactions constrains the climate impact of aviation
Communications Earth & Environment. 2021; **2**, 113 (9 pp.). https://doi.org/10.1038/s43247-021-00175-x

F. Mahrt, E. Newman, Y. Huang, M. Ammann, A. K. Bertram
Phase behavior of hydrocarbon-like primary organic aerosol and secondary organic aerosol proxies based on their elemental oxygen-to-carbon ratio
Environmental Science and Technology. 2021; **55**, 12202-12214. https://doi.org/10.1021/acs.est.1c02697

C. Marcolli, F. Mahrt, B. Kärcher
Soot PCF: pore condensation and freezing framework for soot aggregates
Atmospheric Chemistry and Physics. 2021; **21**, 7791-7843. https://doi.org/10.5194/acp-21-7791-2021

S. M. McNamara, Q. Chen, J. Edebeli, K. D. Kulju, J. Mumpfield, J. D. Fuentes, S. B. Bertman, K. A. Pratt
Observation of N2O5 deposition and ClNO2 production on the saline snowpack
ACS Earth and Space Chemistry. 2021; **5**, 1020-1031. https://doi.org/10.1021/acsearthspacechem.0c00317

A. Mellouki, M. Ammann, R. A. Cox, J. N. Crowley, H. Herrmann, M. E. Jenkin , V. F. Mc Neill, J. Troe, T. J. Wallington
Evaluated kinetic and photochemical photochemical data for atmospheric chemistry: volume VIII - gas-phase reactions of organic species with four, or more, carbon atoms (≥C4)
Atmospheric Chemistry and Physics. 2021; **21**, 4797-4808. https://doi.org/10.5194/acp-21-4797-2021

H. Yang, A. Boucly, J. P. Gabathuler, T. Bartels-Rausch, L. Artiglia, M. Ammann
Ordered hydrogen bonding structure of water molecules adsorbed on silver iodide particles under subsaturated conditions
Journal of Physical Chemistry C. 2021; **125**, 11628-11635. https://doi.org/10.1021/acs.jpcc.1c01767

ANALYTICAL CHEMISTRY

M. Barandun, E. Pohl, K. Naegeli, R. McNabb, M. Huss, E. Berthier, T. Saks, M. Hoelzle
Hot spots of glacier mass balance variability in Central Asia
Geophysical Research Letters. 2021; **48**, e2020GL092084 (14 pp.). https://doi.org/10.1029/2020GL092084

S. O. Brugger, M. Schwikowski, E. Gobet, C. Schwörer, C. Rohr, M. Sigl, S. Henne, C. Pfister, T. M. Jenk, P. D. Henne, W. Tinner
Alpine glacier reveals ecosystem impacts of Europe's prosperity and peril over the last millennium
Geophysical Research Letters. 2021; **48**, e2021GL095039 (12 pp.). https://doi.org/10.1029/2021GL095039

F. Burgay, E. Barbaro, D. Cappelletti, C. Turetta, J.-C. Gallet, E. Isaksson, B. Stenni, G. Dreossi, F. Scoto, C. Barbante, A. Spolaor
First discrete iron(II) records from Dome C (Antarctica) and the Holtedahlfonna glacier (Svalbard)
Chemosphere. 2021; **267**, 129335 (13 pp.). https://doi.org/10.1016/j.chemosphere.2020.129335

L. Fang, T. M. Jenk, T. Singer, S. Hou, M. Schwikowski
Radiocarbon dating of alpine ice cores with the dissolved organic carbon (DOC) fraction
Cryosphere. 2021; **15**, 1537-1550. https://doi.org/10.5194/tc-15-1537-2021

M. Feltracco, E. Barbaro, A. Spolaor, M. Vecchiato, A. Callegaro, F. Burgay, M. Vardè, N. Maffezzoli, F. Dallo, F. Scoto, R. Zangrando, C. Barbante, A. Gambaro
Year-round measurements of size-segregated low molecular weight organic acids in Arctic aerosol
Science of the Total Environment. 2021; **763**, 142954 (10 pp.). https://doi.org/10.1016/j.scitotenv.2020.142954

D. Festi, M. Schwikowski, V. Maggi, K. Oeggl, T. M. Jenk
Significant mass loss in the accumulation area of the Adamello glacier indicated by the chronology of a 46 m ice core
Cryosphere. 2021; **15**: 4135-4143. https://doi.org/10.5194/tc-15-4135-2021

S. Hellmann, J. Kerch, I. Weikusat, A. Bauder, M. Grab, G. Jouvet, M. Schwikowski, H. Maurer
Crystallographic analysis of temperate ice on Rhonegletscher, Swiss Alps
Cryosphere. 2021; **15**, 677-694. https://doi.org/10.5194/tc-15-677-2021

S. Hou, W. Zhang, L. Fang L, T. M. Jenk, S. Wu, H. Pang, M. Schwikwoski
Brief communication: new evidence further constraining Tibetan ice core chronologies to the Holocene
Cryosphere. 2021; **15**, 2109-2114. https://doi.org/10.5194/tc-15-2109-2021

M. Kronenberg, H. Machguth, A. Eichler, M. Schwikowski, M. Hoelzle
Comparison of historical and recent accumulation rates on Abramov Glacier, Pamir Alay
Journal of Glaciology. 2021; **67**, 253-268. https://doi.org/10.1017/jog.2020.103

R. Nardin, M. Severi, A. Amore, S. Becagli, F. Burgay, L. Caiazzo, V. Ciardini, G. Dreossi, M. Frezzotti, S.-B. Hong, I. Khan, B. M. Narcisi, M. Proposito, C. Scarchilli, E. Selmo, A. Spolaor, B. Stenni, R. Traversi
Dating of the GV7 East Antarctic ice core by high-resolution chemical records and focus on the accumulation rate variability in the last millennium
Climate of the Past. 2021; **17**, 2073-2089. https://doi.org/10.5194/cp-17-2073-2021

A. Spolaor, F. Burgay, R. P. Fernandez, C. Turetta, C. A. Cuevas, K. Kim, D. E. Kinnison, J.-F. Lamarque, F. de Blasi, E. Barbaro, J. P. Corella, P. Vallelonga, M. Frezzotti, C. Barbante, A. Saiz-Lopez
Antarctic ozone hole modifies iodine geochemistry on the Antarctic Plateau
Nature Communications. 2021; **12**, 5836 (9 pp.). https://doi.org/10.1038/s41467-021-26109-x

AFFILIATION INDEX

ÅAU	Åbo Akademi University, Tuomiokirkontori 3, 20500 Turku, Finland
Areaphoto	Areaphoto Image & Communication, Via Nevegal 71, 32100 Belluno, Italy
ATMOS	Center for Atmospheric Research, University of Oulu, 90014 University of Oulu, Finland
Bicocca	Università degli Studi di Milano-Bicocca, Piazza dell'Ateneo Nuovo, 1, 20126 Milano, Italy
CNR-ISP	Istituto di Scienze Polari, Ca' Foscari University Venice, Via Torino, 155, 30172 Venice, Italy
CUB	CU Boulder, University of Colorado Boulder, CO 80309, USA
Dolomiti Guides	Guide Alpine Dolomiti Guides, Via Rivinal, 95/c, 32100 Belluno, Italy
ENE	Energy and Environment, Paul Scherrer Institut, 5232 Villigen, Switzerland
EPFL	Ecole polytechnique fédérale de Lausanne, Route Cantonale, 1015 Lausanne, Switzerland
ETHZ	ETH Zürich, Eidgenössische Technische Hochschule Zürich, 8092 Zürich, Switzerland
FHI	Fritz-Haber-Institut der Max-Planck-Gesellschaft, Faradayweg 4-6, 14195 Berlin, Germany
Harvard	Harvard University, Massachusetts Hall, Cambridge, MA 02138, USA
icecrill.ch	icedrill.ch AG, Schützengasse 172, 2502 Biel, Switzerland
INM Minsk	Institute for Nature Management, Laboratory of Transboundary Pollution, National Academy of Sciences of Belarus, Skoriny str. 10, 220076 Minsk, Belarus
IWEP	Institute for Water and Environmental Problems, Ulitsa Molodezhnaya, 1, Barnaul 656038, Altai Krai, Russia
LAC	Laboratory for Atmospheric Chemistry, Paul Scherrer Institut, 5232 Villigen, Switzerland
LBK	Bioenergy and Catalysis Laboratory, Paul Scherrer Institut, 5232 Villigen, Switzerland
LSK	Laboratory for Catalysis and Sustainable Chemistry, Paul Scherrer Institut, 5232 Villigen, Switzerland
LUC	Laboratory of Environmental Chemistry, Paul Scherrer Institut, 5232 Villigen, Switzerland
PhLAM	Laboratoire de Physique des Lasers, Atomes et Molecules, Université de Lille, 2 Avenue Jean Perrin, 59655 Villeneuve d'Ascq Cedex, France
PSI	Paul Scherrer Institut, Forschungsstrasse 111, 5232 Villigen, Switzerland
SBU	Stony Brook University, Department of Chemistry, 100 Nicolls Road, Stony Brook NY 11790-3400, USA
TreaTech	TreaTech, Chemin des Mouettes 1, 1027 Lonay, Switzerland
TROPOS	Leibniz-Institut für Troposphärenforschung, Permoserstrasse 15, 04318 Leipzig, Germany
UBC	The University of British Columbia, Vancouver Campus, 2329 West Mall, Vancouver V6T 1Z4, Canada
UCD	Department of Land, Air and Water Resources, University of California, One Shields Avenue, Davis CA 95616, USA
UGA	Université Grenoble Alpes, 621 Avenue Centrale, 38400 Saint-Martin-d'Hères, France
Univ. Bern	Universität Bern, Departement für Chemie, Biochemie und Pharmazie, Freiestrasse 3, 3012 Bern, Switzerland
Univ. Ca'Foscari	Università Ca'Foscari, Dorsoduro 3246, 30123 Venezia, Italy
ZHdK	Zürcher Hochschule der Künste, Pfingstweidstrasse 96, 8005 Zürich, Switzerland